ENGINEERING

Safe, high-performance, moisture-activated batteries for powering next-generation Internet-of-Things devices

Rajaram Kaveti[1,2]†, Akshay Bhardwaj[1,2]†, Pei Liu[3]†, Ayemeh Bagheri Hashkavayi[1,2]†‡, Bhavya Jain[1,2], Adrian Rodriguez-Kattan[1,2], Mahaboobbatcha Aleem[1,2], Baha Erim Uzunoğlu[1,2], Gurudatt N. G.[1,2], Bünyamin Şahin[1,2]§, Veena Misra[1,2], Raudel Avila[3,4,5]*, Abraham Vázquez-Guardado[1,2]*, Amay J. Bandodkar[1,2,6]*

Conventional batteries are heavy, nonconformal, and toxic, while energy harvesters offer low/variable power, rendering them unsuitable for emerging wearable, robotic, and other Internet-of-Things (IoT) devices. Here, we introduce a nontoxic, thin-film battery superior to several commercial batteries inspired by advances in water harvesting techniques. It scavenges ambient moisture to serve as its electrolyte, combining features of an energy harvester with attractive features of a battery (stable and high power). It functions in a wide range of environments and offers an open-circuit voltage of ~1.6 volts, specific capacity of ~52 milliampere-hours per gram, and specific energy of ~81 milliwatt-hours per gram. Unique pangolin skin–mimicking design imparts high flexibility, stretchability, and fill factor to the battery, ensuring conformability without compromising on capacity. Experimental and computer simulation studies reveal the distinctive materials and design features responsible for the battery's impressive performance. Examples of a wireless wearable pulse oximeter and surveillance monitor with a unique kill switch that secures it from unauthorized access demonstrate the versatility of the battery to power various IoT devices.

INTRODUCTION

Major advances in miniaturized electronics and materials science are paving the way for next-generation wearable electronics (*1*–*3*), robotics (*4*–*6*), and Internet-of-Things (IoT) devices (*7*–*9*). Conventional lithium-ion or alkaline batteries power many of these emerging devices, creating unyielding platforms with stark intradevice mechanical dissimilarity: flexible, miniaturized electronics interfaced with bulky, minimally flexible batteries. These conventional prewetted batteries necessitate the permanent containment of liquid electrolytes, which introduces inherent leakage risks (*10*, *11*). Furthermore, the requirement for rigid, hermetic encapsulation to prevent electrolyte loss substantially increases the dead weight of the device. These factors impose fundamental constraints on the development of lightweight power sources. Moreover, these batteries depend on toxic materials, raising serious health and environmental concerns. Recent examples of nontoxic flexible/stretchable batteries show promise, but their performance is usually subpar compared to commercial batteries (*12*, *13*). In addition, their packaging in thin plastics/elastomers increases electrolyte leakage risks and reduces operational life span. Energy harvesters offer alternatives to batteries; unfortunately, their low, variable energy densities inherently limit their application (*14*, *15*). To overcome these issues, we introduced a class of nontoxic, power sources that combine the stable, high-energy-density feature of batteries with the scavenging attributes of harvesters (*16*). We demonstrated wearable batteries that harvest sweat (*17*, *18*) and later implantable versions that use tissue fluids (*19*) as the electrolyte to power various wireless devices. Several examples of batteries that take inspiration from our ambient liquid-activated battery concept appear in the literature (*20*–*24*). While promising, these batteries only function in scenarios where ambient liquid is readily available, thus limiting their widespread use.

Here, we introduce moisture-activated batteries (MABs) built on a unique battery architecture that addresses the abovementioned challenges. Moisture's omnipresence in all terrestrial regions, from arid to humid areas, expands the use cases for MABs to applications where previously reported ambient liquid-activated batteries cannot be used. The MAB includes a magnesium (Mg) anode and a silver/silver chloride (Ag/AgCl) cathode with an unconventional separator that spontaneously captures moisture from ambient air to serve as a nontoxic electrolyte. The separator is designed to enable rapid activation of the battery cell even under low humidity conditions. The MAB's working principle enables the battery to remain in the "OFF" state when dry (e.g., when it is in its packaging) and activate upon exposure to ambient humidity. A benefit of this mode of operation is suppression of half-cell reactions in the absence of a liquid electrolyte, resulting in negligible self-discharge, which is a major battery issue (*25*, *26*). The unique mechanism, materials, and design enable MAB cells to offer performance that are comparable to, and in some cases exceed, those of commercial batteries under standard operating conditions of 25°C and 50% relative humidity (RH) (table S1) while being composed of materials that are widely used in

[1]Department of Electrical and Computer Engineering, North Carolina State University, Raleigh, NC 27606, USA. [2]Center for Advanced Self-Powered Systems of Integrated Sensors and Technologies (ASSIST), North Carolina State University, Raleigh, NC 27606, USA. [3]Department of Mechanical Engineering, Rice University, Houston, TX 77005, USA. [4]Rice Advanced Materials Institute, Rice University, Houston, TX 77005, USA. [5]Digital Health Institute, Rice University, Houston, TX 77005, USA. [6]Lampe Joint Department of Biomedical Engineering, North Carolina State University and University of North Carolina at Chapel Hill, Chapel Hill, NC 27599, USA.
*Corresponding author. Email: ra88@rice.edu (R.A.); abraham.vg@ncsu.edu (A.V.-G.); ajbandod@ncsu.edu (A.J.B.)
†These authors contributed equally to this work.
‡Present address: Department of Applied Physical Sciences, University of North Carolina-Chapel Hill, Chapel Hill, NC 27599, USA.
§Present address: Department of Basic Sciences, Faculty of Engineering, Necmettin Erbakan University, Konya, Turkey.

biomedical applications (table S2). Table S3 compares the MAB cell's performance to recently reported nontoxic, primary batteries in the literature, illustrating the superiority of the former over conventional, prewetted battery architectures. As a proof of principle, we demonstrate the MAB's ability to power energy-hungry wireless devices with examples involving a wearable pulse oximeter (POx) and a field-deployable, covert surveillance monitor with a unique inbuilt kill switch. This work highlights the key attributes of the MABs that make them a strong contender for replacing legacy batteries for powering a broad range of IoT devices.

RESULTS

Materials and design of MABs

Figure 1A shows the schematic illustration of a MAB. The components of a 2 × 2–unit cell array appear in Fig. 1B. It consists of a flexible Mg anode and a Ag/AgCl cathode. A dry separator, composed of two distinct cellulose-based regions, (i) a capture zone and (ii) an electrolyte zone, is positioned between the two electrodes. The capture zone actively scavenges moisture from the surroundings and condenses it into liquid water. The electrolyte zone then rapidly absorbs this water, establishing an ionically conductive medium between the anode and the cathode, which activates the MAB cell.

Hygroscopic salts such as lithium chloride (LiCl), lithium bromide (LiBr), and calcium chloride ($CaCl_2$) are well known for their moisture-harvesting ability in a wide range of RH conditions (11 to 100% RH) and therefore serve as potential candidates for developing the capture zone (*27*). However, LiCl is one of the most hygroscopic materials, absorbing ~1.35 liters of water per kilogram of salt (*28*), and is characterized by lower relative vapor pressure compared to LiBr and $CaCl_2$, indicating reduced evaporation of the harvested moisture from LiCl-based systems (*27*). The capture zone is therefore composed of a cellulose membrane impregnated with LiCl. While LiCl can also serve as an electrolyte, preliminary studies reveal that a Mg-Ag/AgCl cell with a LiCl electrolyte offers subpar performance compared to an analogous cell with a sodium chloride (NaCl) electrolyte. The areal capacity of a Mg-Ag/AgCl cell with a LiCl electrolyte is ~0.05 mAh/cm^2 compared to nearly 4.2 mAh/cm^2 for an analogous cell with a NaCl electrolyte for a discharge current density of 1 mA/cm^2 and cutoff voltage of 1 V (fig. S1, A and B). Scanning electron microscopy (SEM) images of the Mg electrode after complete discharge of the above two cells may provide an explanation for the differences in the capacity of the two cells. Figure S1 (C and D) shows that the Mg electrode exposed to the LiCl electrolyte is characterized by porous, dendrite-like microstructures. On the other hand, the Mg anode exposed to NaCl reveals the characteristic closely packed, scaly microfeatures of magnesium oxide (*17*). Prior studies investigating aqueous LiCl electrolytes in contact with Mg electrodes reveal that Li ions, because of their smaller size and higher charge density compared to sodium ions, are more efficient at disrupting and solubilizing passivating surface layers such as $MgCl_2$ or $Mg(OH)_2$ on Mg electrodes (*29*, *30*). The more effective disruption of the passivation layers in the LiCl electrolyte leads to faster dissolution of Mg compared to Mg electrodes immersed in the NaCl electrolyte. Linear sweep voltammetry (fig. S1E) and cyclic voltammetry (CV; fig. S1, F and G) experiments test whether lithium-driven faster dissolution of Mg is the underlying reason for the poor capacity of battery cells with the LiCl electrolyte compared to those with NaCl serving as the electrolyte. The setup involves Mg acting as the working electrode, Ag/AgCl as the pseudoreference electrode, and a graphite film as the counter electrode immersed in either 350 mM LiCl or 350 mM NaCl electrolyte. The linear sweep voltammetry study (fig. S1E) reveals that oxidation onset potential for Mg in the LiCl electrolyte is lower (−1.54 V) compared to that for Mg in the NaCl electrolyte (−1.49 V). The CV studies (fig. S1, F and G) also show that the peak oxidation current for the first cycle in the LiCl electrolyte (~5.5 mA) is ~1.8× higher than in the NaCl electrolyte (~3 mA), indicating more rapid oxidation and reduced passivation of Mg in the former compared to the latter. These studies indicate that the Mg anode is more electrochemically active in the LiCl electrolyte than in the NaCl electrolyte, which could be a reason for the poor capacity of LiCl-based cells compared to ones with the NaCl electrolyte. The monotonic decrease in peak oxidation and reduction currents in subsequent CV cycles indicate the irreversible nature Mg plating and stripping in both electrolytes.

Considering the above results, the electrolyte zone is composed of a cellulose membrane preloaded with NaCl. It is further coated with a tacky gel composed of hydroxypropyl cellulose (HPC) and xanthan gum (XG), which facilitates bonding of the electrodes to the electrolyte zone. In addition, the high density of polar groups in these polymers facilitate strong polymer-water interactions, endowing excellent water retention properties (*31*, *32*) to the electrolyte zone essential for maintaining hydration of the separator for optimal battery operation. The two zones are stacked strategically such that the inner edges of the capture zone overlap with the periphery of the electrolyte zone to ensure facile transport of water from the former to the latter. The complete cell is encapsulated within a thin polyethylene terephthalate (PET) membrane. Laser-patterned openings in the PET membrane expose the capture zone to the surroundings for facilitating moisture harvesting. It also helps in expulsing hydrogen gas created at the anode because of side reactions, as shown by us previously (*33*). Figure 1C exhibits a schematic representation of the cross section of a MAB cell. Figure 1D shows an embodiment of a MAB pack (width: 25 mm; length: 25 mm; thickness: 1.8 mm; weight: 0.68 g) consisting of two MABs connected in series with each MAB composed of eight cells in parallel. The pack offers an operating voltage of 3.2 V and a capacity of 50 mAh capable of powering a light-emitting diode (LED) strip (eight LEDs connected in parallel), as shown in Fig. 1E.

The serpentine current collectors connecting the individual cells impart high flexibility and stretchability to the pack (Fig. 1F and movies S1 and S2). The internal structure of the MAB pack without the external silicone packaging is shown in fig. S2. The versatility of the fabrication process also enables creation of cells with standard AA cell form factors that allow direct adoption to powering existing electronics (Fig. 1G, left). Figure S3A illustrates the makeup of the MAB in the AA form factor. A humidity indicator integrated into the MAB provides a real-time visual cue, changing color from blue to light pink upon moisture absorption, thereby signaling battery activation (fig. S3, B and C). Details of the indicator appear in our prior work (*33*). MAB cells outperform commercial cells when comparing the specific capacity, specific energy, and open circuit voltage owing to their unique working principle and choice of materials (Fig. 1G, right, and table S1).

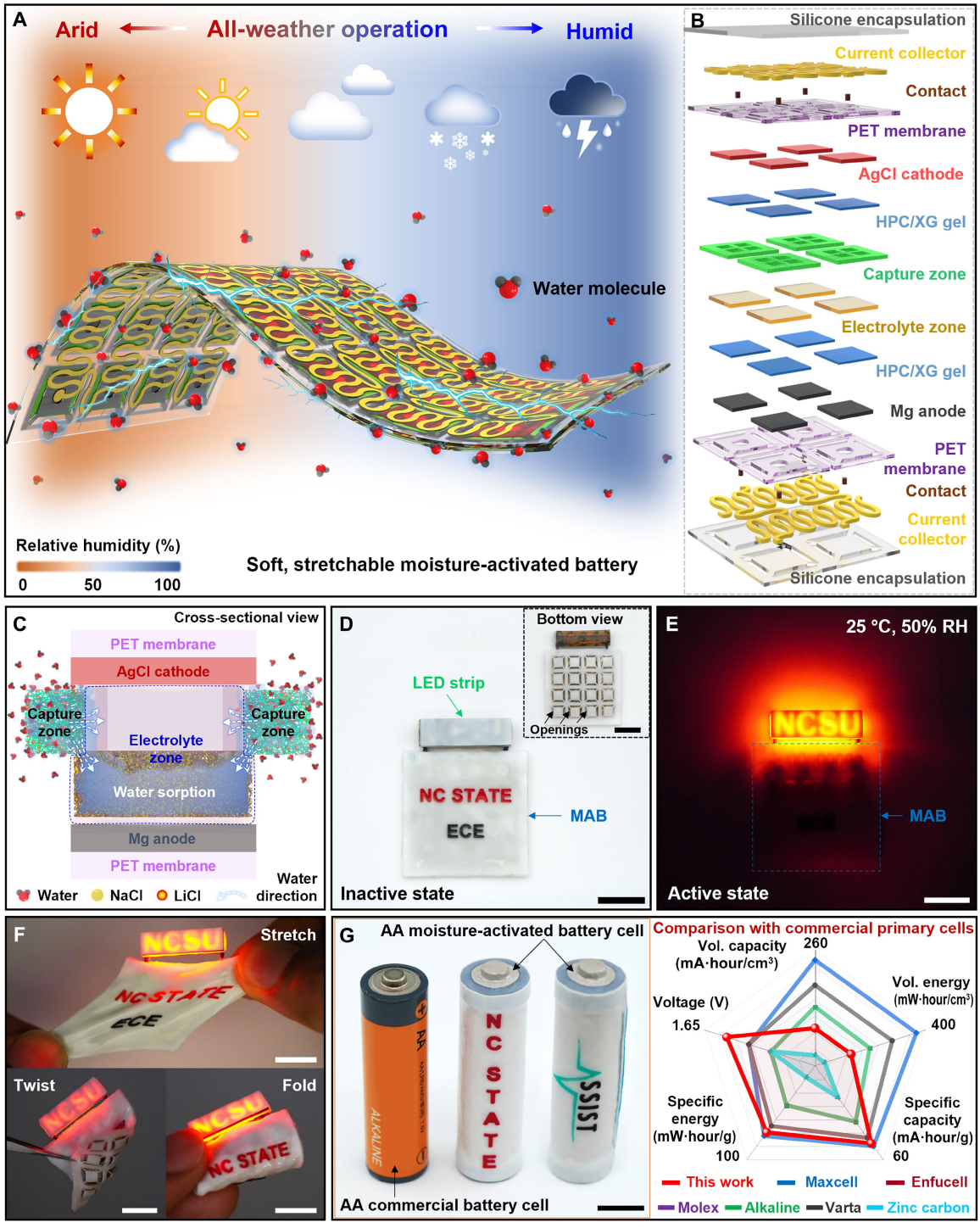

Fig. 1. Materials, design, and performance characteristics of soft, stretchable MAB. (**A**) Schematic illustration of the soft and stretchable MAB designed to operate reliably across a wide range of environmental conditions, from arid to humid climates. (**B**) Exploded view of a 2 × 2 unit cell array, detailing the structural design and constituent materials of each layer. (**C**) Schematic highlighting the working principle of the MAB's separator consisting of a capture zone and electrolyte zone. The capture zone scavenges and phase transitions ambient moisture vapors to liquid water; the electrolyte zone absorbs the liquid and dissolves the preloaded NaCl salt to serve as the electrolyte. (**D**) Photographs of an inactive, fully assembled 4 × 4 cell array encapsulated within an elastomeric membrane capable of powering an LED strip encapsulated using a light diffuser with an NCSU logo. The inset shows the battery's rear side, featuring moisture ingress openings. (**E**) Photograph of a fully active MAB powering the LED strip under ambient condition (25°C and 50% RH). (**F**) Images demonstrating the ability of the soft MAB to maintain functionality during stretching, twisting, and folding stressors. (**G**) Image showing a commercial AA-sized battery cell (left) and AA-sized MAB cell (center and right) and radar plot comparing performance metrics of the MAB cell with those of commercial primary battery cells under optimal operating conditions (25°C and 50% RH) for both groups. The volume and mass of the MAB cell used for calculating the parameters are measured after the separator is fully hydrated. [(D) to (G)] Scale bars, 1 cm.

Mechanical characteristics and finite element analysis of MAB

The MAB is made of inherently rigid materials. A widespread approach to imparting flexibility and stretchability to such systems involves designing the system with island-bridge features wherein the rigid materials are mounted on the islands that are interconnected with stretchable serpentine bridges (*34*–*37*). While such designs impart exceptional conformability to rigid systems, they are unsuitable for achieving high-areal-capacity batteries (*37*–*39*). To address this issue, the MAB takes inspiration from pangolin's skin. The pangolin skin–inspired soft MAB tightly packs individual rigid cells on a biaxially stretchable serpentine current collector in a manner that allows a fill factor of 87% while still facilitating high flexibility and biaxial stretchability. Figure S4 (A and B) shows the schematic representation of the pangolin skin–inspired 2 × 2 array MAB structure with a high fill factor compared to conventional design for incorporating conformability to the device.

Figure 2 summarizes the mechanical and electrical responses of a MAB comprising 4 × 4 individual cells under various deformation modes, with optical images and finite element analysis (FEA) simulations showing strong alignment. Bending simulations along the *z* axis reveals strain localization along the central axis with peak strains <5% at the smallest radius of curvature (Fig. 2A). Diagonal bending (Fig. 2B), achieved through compression of the corner cells, results in a more uniform strain distribution along the serpentine, with maximum strain values <3%. The serpentine interconnects undergo out-of-plane buckling at high strains (≥60%) under uniaxial and biaxial stretching (up to 80%) to dissipate localized stresses (figs. S5, A and B, and S6). Additional bending mechanics analysis along both *x* and *y* as well as diagonal bending directions appear in fig. S7. Bending the MAB with curvature radii of 10, 15, and 20 mm reveals anisotropic mechanical behavior arising from the serpentine interconnect's geometry with principal strains approaching ~10% along the *x* axis compared to <5% along the *y* axis. This design reflects the directional mechanics compliance embedded in the serpentine design to accommodate complex deformations. Furthermore, the diagonal bending response varies with different principal bending directions because of the anisotropic nature of the serpentine design (fig. S7, C and D). FEA also captures the mechanical stretchability of the MAB under complex loading conditions (fig. S8, A and B). Simulated strain distributions show close agreement with experimental deformations, with maximum strains in the serpentine layer <7%, localized at the arc regions of the serpentine interconnects from out-of-plane deformation within the battery architecture.

Figure 2C presents the electric field distribution in the interconnects and corresponding resistance changes under bending, twisting, and stretching deformations. The applied mechanical loads are normalized as $\frac{\varepsilon_x}{\varepsilon_{max}}$, $\frac{U_x}{U_{max}}$, $\frac{\phi}{\phi_{max}}$ for comparison and detailed in Materials and Methods. During *y*-axis bending (curvature: 0.01 to 0.5/mm), *x*-axis twisting (angle: 0 to 2π radians), and *y*-axis stretching (strain: 0 to 90%), the relative resistance change ($\Delta R/R_0$) in the interconnects is <0.1%. Under extreme uniaxial strain (90 to 200%), $\Delta R/R_0$ increases to 0.7%, highlighting the high electromechanical stability of the interconnects under complex deformation (*35*, *40*, *41*). FEA further reveals that strain localizes primarily within the serpentine interconnects, while the rigid cells remain largely unaffected. This strain isolation and minimal resistance variation stem from geometry-driven stretchability rather than intrinsic material elongation. The above studies reveal that serpentine interconnects enable modular stretching between densely packed cells while maintaining electrical continuity and avoiding material or structural failure owing to its unique pangolin skin–inspired structure.

Characterization of the hygroscopic separator

Figure 3A shows the schematic illustration of the hygroscopic separator. Figure 3B investigates the influence of LiCl loading in the capture zone on its dynamic moisture sorption capabilities at 25°C and 50% RH. The data reveal that the capture zone's moisture absorption property increases with increasing LiCl loading, with a loading of 30 mg/cm^2 scavenging nearly 55 μl/cm^2 ambient moisture. Figure S9 shows longitudinal water uptake capability for the capture zone with 30 mg/cm^2 LiCl at 70% RH and 25°C. Loading >30 mg/cm^2 compromises the capture zone's mechanical integrity. Therefore, the capture zone with a LiCl loading of 30 mg/cm^2 is selected for all future studies. Time-dependent FEA of ambient moisture absorption in the capture zones predicts the weight change and saturation for variable LiCl loadings. Simulations accurately reproduce experimental results with error <9% and capture the initial rapid weight increase characteristic of the onset of moisture absorption governed by Eq. 5 (see Materials and Methods). Dynamic moisture sorption capabilities are modeled empirically by Eq. 6 (see Materials and Methods), a second-order function calibrated from experiments, to bridge the nanoscale water and LiCl molecule interactions to the mesoscale capture zone weight changes that reflect the enhanced sorption of higher LiCl loadings.

Figure 3C visually shows the separator's ability to readily scavenge and condense ambient moisture to liquid water in the capture zone and then transport it to the electrolyte zone at 25°C and 50% RH. Here, the capture zone is structured by laser-cutting the cellulose membrane with four circular collection pads connected by thin bridges to help maintain the positions of the collection pads while assembling the separator. The square-shaped electrolyte zone [preloaded with 2.4 mg/cm^2 NaCl per our prior work (*17*)] is placed on top of the capture zone, and the two layers are encapsulated by a thin PET membrane. Figure S10A shows the schematic of the separator developed for testing unidirectional water transport from the capture zone to the electrolyte zone. The initially dry capture zone rapidly harvests ambient moisture and routes water to the electrolyte zone within 10 min, and the latter is saturated with water within 90 min as visually illustrated by the spreading of the red dye from the capture zone to the electrolyte zone. Such rapid hydration of the electrolyte zone can be attributed to the highly hygroscopic nature of the capture zone coupled with the high pumping and water retention property of the electrolyte zone imparted by the HPC/XG gel's chemical potential gradient and its porous morphology, which expands and stores water during water sorption, as previously described by a two-concentration model for hygroscopic gels (*42*). SEM images of dry (Fig. 3D) and fully hydrated (Fig. 3E) electrolyte zones provide proof for this explanation. The pristine, dry gel is densely packed with small pores, which swell upon water sorption, resulting in large pores that store the captured water.

FEA simulations corroborate experimental observations, confirming directional and time-dependent water transport under 30% RH conditions (fig. S10B). Simulated transport profiles at 10, 30, and 90 min reveal the evolving spatial distribution of water within the cellulose membranes, demonstrating the saturation and transport within the system. The overall uptake dynamics are then governed by the coupled processes of capture-driven moisture influx and storage

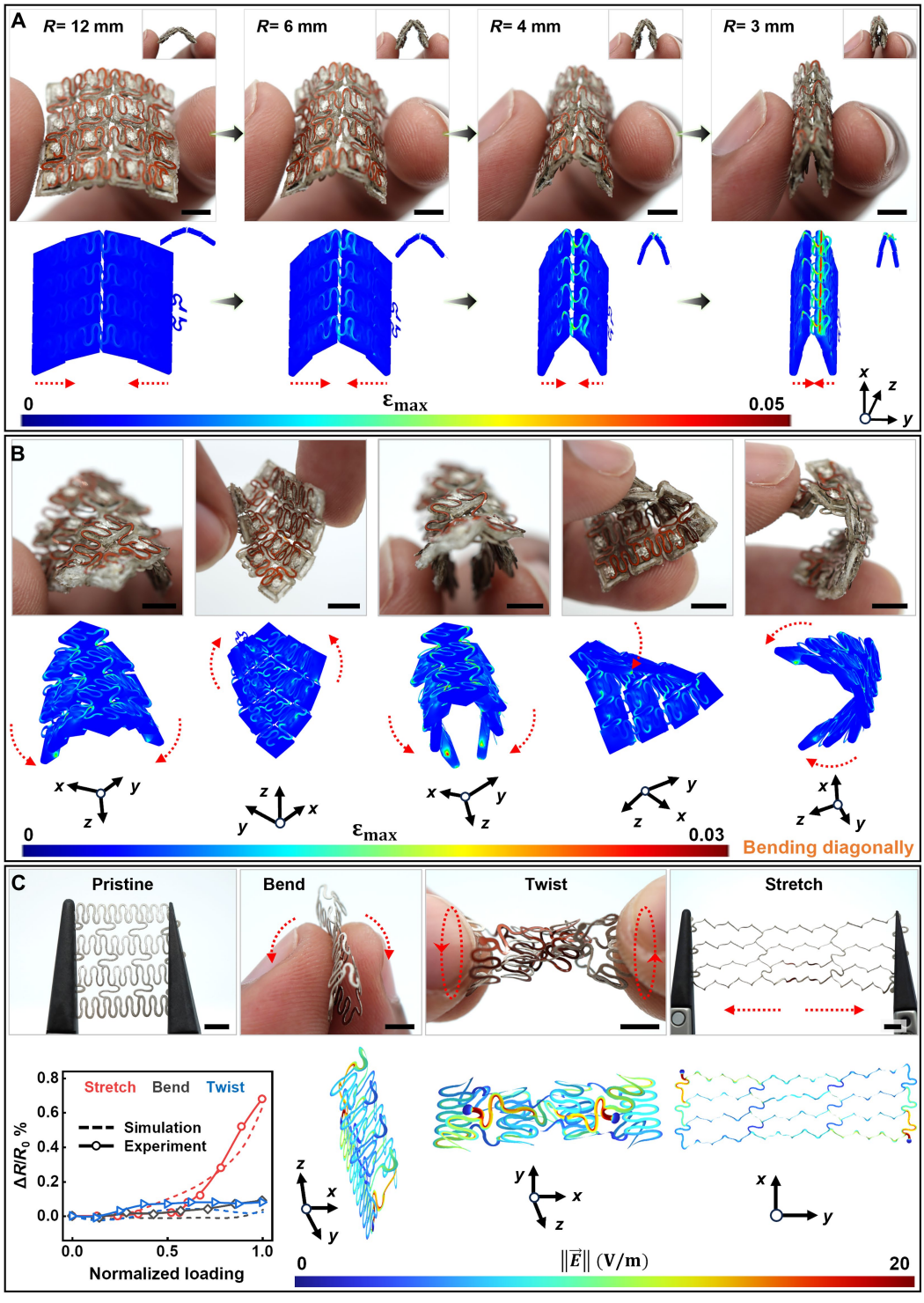

Fig. 2. Experimental and theoretical characterization of mechanical and electrical characteristics of the MAB. Photographic (top) and corresponding 3D-FEA (bottom) images of a 4 × 4 cell array under (**A**) symmetric (compressive stress) and (**B**) antisymmetric diagonal (compressive and tensile stress) bending states for various levels of applied strain. (**C**) Photographs (top), corresponding 3D-FEA (bottom right), and experimental and simulated percentage change in resistance of serpentine interconnects under various levels of applied strain (bottom left). All data are presented as the means ± SD; $n = 4$. [(A) to (C)] Scale bars, 5 mm.

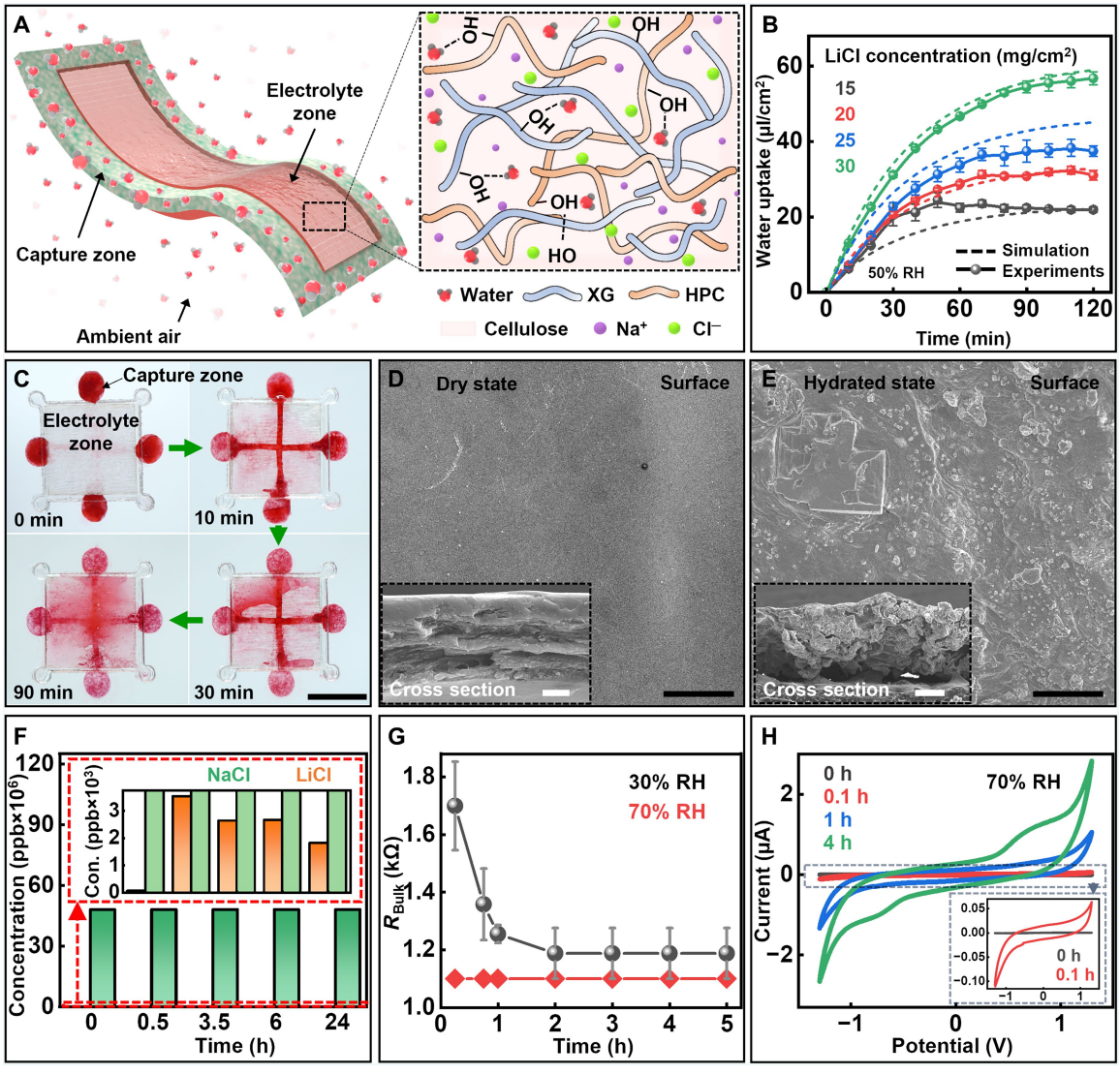

Fig. 3. Characterization of the hygroscopic separator. (**A**) Schematic depicting the hygroscopic separator's working principle and material composition. It consists of a capture zone made of a cellulose membrane loaded with LiCl and an electrolyte zone made of a NaCl-loaded cellulose membrane coated with HPC/XG gel. The inset shows a zoomed-in illustration of the electrolyte zone. (**B**) Plot comparing experimental and simulation results quantifying water uptake over time by the capture zone with LiCl concentrations ranging from 15 to 30 mg/cm^2 under ambient conditions of 25°C and 50% RH. (**C**) Photographs showing time-dependent water transfer from the capture zone (LiCl loading: 30 mg/cm^2) to the electrolyte zone (NaCl loading: 2.4 mg/cm^2) visually observed by the transport of the red dye from the former to the latter under ambient conditions of 25°C and 50% RH. SEM image showing the surface morphology of (**D**) a pristine, dry gel and (**E**) a fully hydrated gel. The insets show the corresponding cross-sectional view. (**F**) ICP-MS analysis of the amount of diffused lithium from the capture zone to the electrolyte zone in the hygroscopic separator over 24 hours (h). The inset shows the magnified bar plot. ppb, parts per billion. (**G**) EIS plots of the separator's bulk resistance as a function of time at 25°C (ambient humidity: 30 or 70% RH). (**H**) CV curves showing the evolution of the electrochemical window of the separator at 25°C and 70% RH (voltage range: −1.3 to +1.3 V; scan rate: 100 mV/s). The inset shows the magnified curves at times of 0 and 0.1 hours. All data are presented as the means ± SD; $n = 4$. (C) Scale bars, 5 mm; [(D) and (E)] scale bars, 250 μm; [(D), inset, and (E), inset] scale bars, 10 μm.

within the swelled volume of the electrolyte zone. Experimental and simulation studies across different RH conditions (Fig. 3C and figs. S10 and S11) further show that the effective diffusivity of the cellulose, shown in Eq. 7 (Materials and Methods), accelerates hydration kinetics, particularly under dry environments. As expected, elevated humidity levels (70% RH) substantially augment the hydration process of the electrolyte zone with the entire zone fully hydrating in less than 20 min, as demonstrated experimentally (fig. S11A) and via simulations (fig. S11B). These modeling results establish a rational basis for optimizing the separator structure and materials to achieve rapid, directional hydration.

As fig. S1 demonstrates, LiCl deleteriously affects the performance of the MAB. Therefore, preventing LiCl leaching from the capture zone into the electrolyte zone is crucial. To investigate the extent of LiCl leaching, fully assembled separators are exposed to ambient air (50% RH; 25°C) for varying periods of time up to 24 hours. Removal of the electrolyte zone from the separator and analyzing it via inductively coupled plasma mass spectrometry (ICP-MS) help quantify the

diffusion of lithium ions in the electrolyte zone. Figure 3F and fig. S12 reveal negligible diffusion of lithium ions into the electrolyte zone over the entire duration of the study. This observation may be attributed to the in situ formation of a saturated NaCl solution in the electrolyte zone upon hydration. This saturated solution impedes the flow of additional ions, such as lithium and chloride ions, from the capture zone into the electrolyte zone. A closer look at the results shows an initial rise followed by a drop in lithium-ion concentration within the electrolyte zone. The initial increase in the lithium-ion concentration is indicative of transient diffusion driven by the concentration gradient of LiCl between the capture and electrolyte zones during the hydration of the separator. The subsequent depletion of the measured lithium-ion concentration over extended durations is likely attributable to dilution resulting from continuous water uptake by the separator. Consumption of lithium ions at the anode is not expected because of the lower oxidation potential of lithium compared to Mg. Crucially, from the MAB cell performance perspective, ICP-MS analysis reveals that the cumulative lithium-ion concentration over the entire 24-hour evaluation remains approximately four orders of magnitude lower than the sodium-ion concentration in the electrolyte zone. Consequently, the influence of diffused lithium ions on the overall electrochemical performance of the MAB cell is negligible.

The MAB cell's internal resistance evolves on the basis of the state of the hydration of its separator. This dynamic resistance directly influences the cell's performance and capacity. Electrochemical impedance spectroscopy (EIS) helps deconvolve the bulk (R_{bulk}) and interfacial ($R_{interfacial}$) resistances of the electrolyte zone, enabling the study of separator resistance as a function of exposure time to ambient moisture. For these studies, a system composed of a separator sandwiched between a pair of printed carbon electrodes (selected for their electrochemical inertness) is used. Figure 3G illustrates the evolution of R_{bulk} for this system. In a 30% RH environment, the initial R_{bulk} of ~1.7 kΩ drops rapidly, stabilizing at ~1.2 kΩ after 2 hours. As expected, the separator placed at 70% RH fully hydrates in <5 min (the duration of a single EIS scan), exhibiting a nearly stable R_{bulk} of ~1.1 kΩ.

Figure S13A reveals a more detailed analysis and complex impact of the HPC/XG gel on the bulk and interfacial resistance (R_{bulk} and $R_{interfacial}$) of the electrolyte zone. This study is conducted using a system similar to that of Fig. 3G, except that the separator consists exclusively of the electrolyte zone. Controlled hydration of the separator is achieved by progressively adding increasing known volumes of water in the separator. Capturing Nyquist plots after each addition allows investigation of the evolution of R_{bulk} and $R_{interfacial}$ as a function of the volume of water in the electrolyte zone. Initially, both separators, with and without the gel, exhibit immeasurable resistance by EIS when they are in a pristine, dry state. The addition of just 4 μl/cm^2 water results in measurable R_{bulk} and $R_{interfacial}$ values for both separators. The strong water sorption properties of the gel facilitate rapid and nearly complete hydration of the bulk of the separator with only 4 μl/cm^2 water. This is reflected in a low R_{bulk} of ~810 Ω for the gel-containing separator, which remains nearly constant regardless of the extent of hydration of the separator. In contrast, the R_{bulk} for the separator without the gel starts at a higher value of ~2.8 kΩ for 4 μl/cm^2 water. This resistance progressively decreases and stabilizes at ~1.1 kΩ after the separator is loaded with around 10 μl/cm^2 water, indicating that the separator without the gel requires nearly twice the volume of water for complete hydration.

For both separators, the evolution of $R_{interfacial}$ reveals that interfacial resistance decreases with increasing water content. However, the separator without the gel shows a more pronounced decrease in $R_{interfacial}$ compared to the gel-containing one. The former stabilizes at ~2.5 MΩ, while the latter stabilizes at a higher value of ~27 MΩ. A collective analysis of the R_{bulk} and $R_{interfacial}$ results indicates that the gel-containing separator hydrates the bulk of the separator more effectively than the electrode-separator interface. Conversely, the separator without the gel concentrates water at the interface, keeping the bulk drier relative to the gel-based separator. The data reveal that the separator must capture mere 10 μl/cm^2 ambient moisture to achieve an electrochemically stable separator. The lower interfacial water content and rapid bulk hydration observed in the gel-containing separator are beneficial as the former helps reduce electrode corrosion, while the latter reduces the battery's internal resistance. These effects collectively result in improved battery performance, as discussed later.

Results of experiments investigating the effect of HPC/XG gel thickness on the MAB cell's areal capacity appear in fig. S13B. The areal capacity increases from ~19.2 mAh/cm^2 for a 50-μm-thick gel to ~24.7 mAh/cm^2 for cells with a 100-μm-thick gel before decreasing to ~16.7 mAh/cm^2 for those with a 200-μm-thick gel. When the gel layer is relatively thin (<100 μm), the limited water-holding capacity may be insufficient to sustain hydration during prolonged discharge, potentially leading to partial dehydration, reduced ionic conductivity, and diminished capacity. Conversely, excessively thick gel layers (>100 μm) could increase the effective ionic diffusion length and may exacerbate interfacial resistance at the electrode-separator interface, thereby slowing electrochemical kinetics and reducing the capacity. On the basis of these observations, an intermediate gel thickness of ~100 μm appears to provide a favorable balance between moisture retention and ionic transport while avoiding excessive resistive losses. Per results shown in fig. S13A, a minimum of 10 μl/cm^2 water must be present in the electrolyte zone for achieving a stable separator. Studies shown in Fig. 3B and fig. S9 reveal that the separator requires ~8 and 6 min to capture 10 μl/cm^2 water when the ambient RH values are 50 and 70%, respectively. These studies collectively indicate that MAB cells can provide stable performance within ~7 min of exposure to ambient moisture under typical operational conditions (25°C; RH: 50 to 70% RH).

CV is used to further study the dynamic electrode-separator interface using a system similar to that of Fig. 3G. A featureless, flat CV plot is obtained initially when the separator is almost dry (Fig. 3H). Within 5 min of exposure to ambient air (25°C and 50% RH), the separator produces a characteristic CV plot typical for a system with no redox-active molecules. As the time progresses, the forward and reverse scans enlarge because of the increased ionic conductivity of the separator resulting from increased hydration of the separator (fig. S14). A stable CV signal is obtained ~4 hours after the separator's exposure to ambient moisture. While the CV experiments show that a ~4-hour period is needed for stable ionic conductivity, the MAB functions effectively even without full stability, as shown later.

Characterization of MAB cells

Figure 4A shows the areal capacities of cells with varying amounts of LiCl loaded in the capture zone. An incubation period (defined as the duration of exposure of a cell to ambient air before discharge) of 2 hours is implemented to allow sufficient time for activation. The

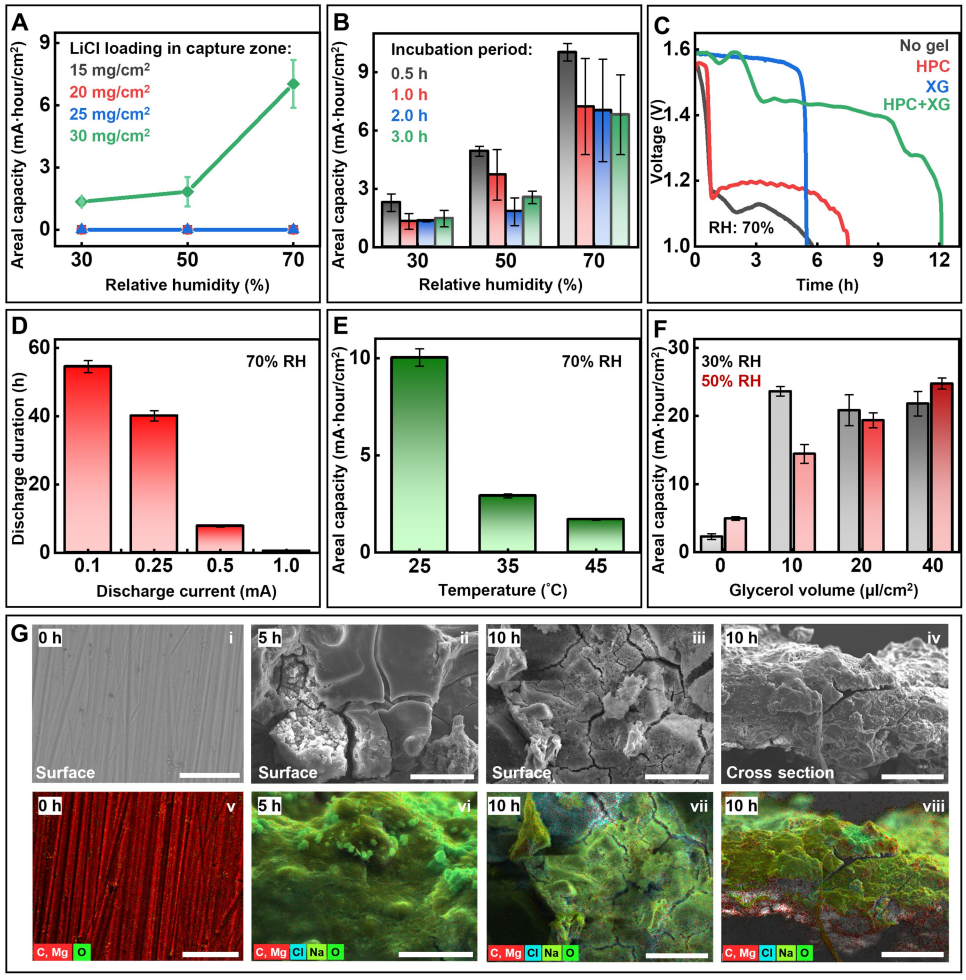

Fig. 4. MAB discharge properties and microstructural analysis. (**A**) Effect of the capture zone's LiCl loading on the MAB cell's areal capacity (incubation period: 2 hours). (**B**) Influence of incubation period and ambient humidity on the areal capacity of MAB cells. (**C**) Effect of different gel compositions in the electrolyte zone on the discharge properties of MAB cells. (**D**) Effect of discharge current on the discharge duration of MAB cells. (**E**) Effect of ambient temperature on the areal capacity of the MAB cells. (**F**) Effect of the separator's Gly concentration on the MAB cell's areal capacity under ambient humidity values of 30 and 50% RH. (**G**) SEM images (top) and corresponding EDX images (bottom) of the surface and cross section of the Mg anode at various discharge intervals of MAB cells. [(A) to (F)] MAB cell size: 5 mm by 5 mm; LiCl loading in the capture zone: 30 mg/cm^2; NaCl loading in the electrolyte zone: 2.4 mg/cm^2; incubation period: 30 min; discharge current: 1 mA/cm^2; cutoff voltage: 1 V; ambient humidity: 50% RH; ambient temperature: 25°C, unless specified. All data are presented as the means ± SD; $n = 4$. [(G), i to iii, v, and vii] Scale bars, 50 µm. [(G), iv and viii] Scale bars, 250 µm. [(G), vi] Scale bar, 25 µm.

cells' voltage with LiCl loadings up to 25 mg/cm^2 almost immediately falls below 1 V probably due to the inability of the capture zone to harvest sufficient moisture, as visually confirmed by the near-dry electrolyte zone. In contrast, MABs with a LiCl loading of 30 mg/cm^2 progressively offer higher capacities as ambient humidity increases, with the capacity approaching 7 mAh/cm^2 at 70% RH. On the basis of these results and those reported in Fig. 3B, MABs with capture zones loaded with 30 mg/cm^2 LiCl are used for all future studies.

Figure 4B shows the effect of incubation period on the cells' performance under different ambient humidity levels. The cells offer the highest capacities for a 30-min incubation period with capacities showing an inverse relationship with incubation period. This trend likely arises from moisture-induced corrosion of Mg and excess electrolyte solvation, which compromise MAB's electrochemical stability and limit its performance. Hence, an incubation period of 30 min is selected for all future tests. Figure 4C highlights the significance of HPC/XG gel in enhancing battery capacity. The discharge curves show that the MAB cell with HPC/XG gel offers 2.1- and 1.6-fold higher capacity compared to those without the gel or single-component gel (HPC or XG), respectively. This enhancement may be attributed to the synergistic interaction between the two polymers, which enhances the HPC/XG gel's water uptake properties. Further analysis of the discharge curves reveals that the cell with XG gel offers more stable output voltage, albeit lower capacity, compared to that with HPC/XG gel. The precise mechanisms underlying the voltage stability disparity between HPC/XG and XG-only systems require further elucidation. From an application standpoint, most integrated electronics, including those demonstrated later in this work, remain robust against transient voltage fluctuations, provided that the supply voltage remains above the microcontroller's operational cutoff voltage. Therefore, all subsequent studies involve MAB cells with HPC/

XG gel to prioritize cells with higher overall capacity over those with more stable output voltage.

Figure 4D demonstrates the MAB cell's discharge duration as a function of discharge current. Figure 4E shows the effect of ambient temperature on the cell's capacity, which decreases with increasing temperature. This decrease is primarily driven by enhanced water evaporation from the separator and accelerated corrosion of Mg under elevated temperatures. To suppress evaporative losses, glycerol (Gly) is added to the HPC/XG gel given that it improves XG's water retention ability (*43*). Gly also imparts corrosion inhibition properties to Mg (*44*, *45*). Gly's influence on the cell's capacity is shown in Fig. 4F, revealing a ~10× increase in capacity compared to cells without Gly. Real-time EIS for systems composed of separators with and without Gly sandwiched between pairs of printed carbon electrodes (similar to the setup in Fig. 3G) reveal the effect of Gly on separator resistance. The corresponding R_{bulk} and $R_{interfacial}$ extracted from the Nyquist plots are presented in fig. S15 (A and B). At $t = 0$ hours, both systems exhibit comparable R_{bulk} (~3 to 4 kΩ). As hydration proceeds, R_{bulk} for both systems rapidly decreases and stabilizes at ~0.7 kΩ after ~1 hour. These values are consistent with those reported in Fig. 3G and fig. S13A, confirming that Gly does not adversely affect bulk ionic transport. In contrast, a pronounced difference is observed in the $R_{interfacial}$ for the two systems. The $R_{interfacial}$ is initially high (~30 MΩ at $t = 0$ hours) for the separator with HPC/XG gel, which rapidly decreases and stabilizes to ~7 MΩ by $t = 1$ hour, reflecting poor interfacial wetting and charge transfer. By comparison, the separator with Gly/HPC/XG gel exhibits a markedly lower $R_{interfacial}$, measuring ~0.4 kΩ at $t = 0$ hours that further decreases to ~0.2 kΩ after 2 hours. These studies demonstrate that Gly reduces the overall internal resistance of the cell by preserving bulk ionic conductivity while significantly reducing interfacial resistance. The observed behavior can be rationalized by Gly's plasticizing role. Prior studies show that Gly forms extensive hydrogen-bonded networks with polymer matrixes (here, HPC/XG), increasing free volume and enhancing polymer segmental mobility (*46*, *47*). This effect promotes ion dissociation and ion transport, reduces interfacial polarization, and facilitates rapid wetting of electrode-electrolyte interfaces that result in improved ionic conductivity of the separator as shown by a prior work that reports a 145-fold increase in ionic conductivity upon incorporation of 25 wt % Gly in a cellulose-based separator (*48*).

The observed cell performance matches and, in some cases, surpasses those of several commercial primary cells under standard conditions of 25°C and 50% RH (table S1). Additional experiments evaluating the effect of Gly on the MAB cells' performance under extreme environmental temperatures (−20° and +60°C) and humidity (10 and 100% RH) appear in fig. S15 (C to F). Mean areal capacities for the MAB cells under extreme and standard conditions (25°C and 50% RH) are compared in table S4 (with Gly) and table S5 (without Gly). The performance attenuation observed at −20°C compared to that at 25°C and 50% RH is likely attributable to decreased ionic mobility within the electrolyte and sluggish redox kinetics, although the precise mechanisms warrant further investigation. Similarly, the decrease in capacity under extreme conditions is expected. At 10% RH, slow or incomplete hydration of the separator likely increases internal ohmic resistance, whereas conditions of high humidity (100% RH) and elevated temperature (60°C) may accelerate parasitic Mg oxidation. It should be noted that the performance of MAB cells even under these extreme conditions is still superior to that of many recently reported nontoxic batteries operating under optimal conditions (25°C; see table S3). While datasheets for commercial batteries specify the range of safe operating conditions (typically −20° to +60°C and 20 to 90% RH), they fail to provide performance data under these specific extremes. Consequently, a direct benchmarking of the MAB cells against commercial counterparts under extreme conditions is challenging because of the absence of vendor-supplied metrics. Our studies reveal that the MABs are safe to use within these extreme temperature and RH ranges, and they offer the best performance around 25°C and in the 30 to 50% RH range, similar to commercial batteries.

Figure S16A reveals the MAB cell's performance under dynamically varying ambient RH. The experiment involves introducing MAB cells in a controlled environment chamber initially maintained at 80% RH and 25°C and discharging them while the RH of the chamber is continuously decreased at the rate of ~20% RH/hour to a final value of 10% RH. As shown in fig. S16A, the cell exhibits substantial voltage stability despite substantial changes in ambient RH level. Specifically, the cell voltage decreases only marginally from 1.58 to 1.57 V when the ambient humidity decreases from 80 to 50% RH over a period of 1.5 hours and to 1.52 V when the humidity further reduces to 10% RH over the next 2 hours, corresponding to a total voltage reduction of ~3.8% over the entire RH range. This decrease in the voltage over 3.5 hours is similar to that observed for battery cells under constant ambient RH conditions (e.g., 2.5 and 7.7% decreases in output voltage over 3.5 hours for cells maintained at constant 50 and 30% RH, respectively). Such performance stability highlights the MAB cell's advantage particularly for real-world wearable and field-deployable applications, where ambient RH levels can vary substantially during operation.

Figure S16B shows data for studies pertaining to investigating the effect of total water content in the electrolyte zone on the MAB cell's capacity. These studies involve cells composed of separators with only the electrolyte zone. The cells are activated by applying varying quantities of water to the separator followed by discharging them at 1 mA/cm^2 (cutoff voltage: 1 V; 25°C and 50% RH). As shown in fig. S16B, increasing the amount of water in the electrolyte zone leads to a systematic increase in areal capacity from ~7.4 to ~12 mAh/cm^2 for cells activated with 5 and 30 μl/cm^2 water, respectively. The lower capacity reported for cells activated with 30 μl/cm^2 water compared to moisture-activated cells that are composed of the complete separator (capture zone and electrolyte zone) can be attributed to faster evaporation of water from the former compared to the latter, wherein the capture zone continually hydrates the electrolyte zone, thus maintaining effective ionic mobility and lower internal resistance. The initial operating voltage for all cells is ~1.5 V before gradually decreasing as the cell discharged. The voltage for cells activated with <5 μl/cm^2 water immediately drops below 1 V when discharged at 1 mA/cm^2. These results demonstrate that the absorbed water content directly governs ionic conductivity and interfacial wetting during activation, thereby controlling the cell's discharge properties in the nonsteady regime. Figure S16C displays the MAB cell's areal power density across varying external loads at 50 and 10% RH. The data show that ambient humidity negligibly affects the areal power density for loads >10 kΩ. However, it decreases noticeably for cells powering low-resistance loads (<10 kΩ) in low ambient humidity conditions (10% RH) compared to those operating in typical humidity scenarios (50% RH). Figure 4G and fig. S17A present the morphological and elemental analyses of the anode before and after discharge. SEM

images and energy-dispersive x-ray spectroscopy (EDX) analysis show progressive crack formation and elevated levels of sodium, chloride, and oxygen, indicating pervasive corrosion and oxide formation throughout the anode structure as the cell discharges. Figure S17B presents an EDX image of the cross section of the HPC/XG gel collected after a 10-hour battery cell discharge. On the basis of the two-dimensional elemental map, Mg is predominantly localized at the gel boundary directly in contact with the anode. Conversely, sodium and chloride are concentrated at the interface between the gel and the cellulose membrane of the electrolyte zone. This spatial separation demonstrates that the gel functions as a diffusion barrier, effectively impeding the migration of Mg ions from the anodic reaction and sodium and chloride ions from the NaCl-loaded cellulose membrane. This is critical for mitigating chloride-induced corrosion on the Mg anode and preventing cathode poisoning by Mg ions. The ability of the gel to act as an ionic barrier may also help explain higher interfacial resistance recorded for a gel-containing separator, as shown in fig. S13A. Collectively, these results demonstrate the gel's ion diffusion barrier capability, which effectively mitigates corrosion and cathode poisoning.

Results reported in fig. S18 illustrate the effect of long-term storage on MAB cell capacity. The study involves vacuum-sealed packaging of freshly fabricated MAB cells with and without Gly in the separator and storing the packaged cells at 25°C and 50% RH for 15 days (fig. S18A). Discharging the cells after the 15-day-long storage period reveals that MAB cells without Gly in the separator retain substantial discharge capacity compared to those with Gly. Specifically, the cells without Gly offer an areal capacity of ~8.52 mAh/cm^2 (fig. S18B), corresponding to only ~1.04% lower areal capacity compared to freshly prepared cells. In contrast, cells containing Gly offer ~4.2 mAh/cm^2 (fig. S18B), representing ~83% reduction in areal capacity relative to freshly prepared cells. This decrease in performance can be attributed to the aqueous and highly polar nature of Gly that may cause undesired half-cell reactions during the OFF state. Figure 4F and fig. S13A show that Gly lowers internal battery resistance and improves battery capacity by reducing water evaporation from the electrolyte zone and augmenting ionic mobility for freshly prepared MAB cells. However, results in fig. S18B reveal that it also compromises long-term stability by facilitating Mg corrosion and parasitic reactions during the OFF state, leading to degraded shelf-life and storage capacity. Future work should focus on replacing Gly, a liquid hygroscopic material, with solid hygroscopic materials [e.g., metal-organic frameworks (*49*)] that can potentially offer complete suppression of the half-cell reactions during storage and enable realization of MAB cells with long storage life.

MAB-powered, next-generation, IoT devices

The high voltage (1.6 V), specific energy (81.5 mWh/g), and specific capacity (52.6 mAh/g) of the MAB cells in conjunction with a strategic power management circuitry enable powering a rich variety of IoT devices with demanding voltage and current requirements. Examples include a wireless POx for personalized health monitoring and a field-deployable, covert surveillance monitor for environmental monitoring. Both systems rely on Bluetooth Low Energy (BLE)—a communication protocol with a high dynamic loading characteristic (~16-mA/44.8-mW peak current/power demand in 0.1-ms transients or 6.38-mA/17.9-mW average currents/power over 7.5-ms Bluetooth Rx/Tx events). The main modules of the demonstrator devices are (i) a BLE microcontroller (CC2640R2F, Texas Instruments), (ii) a 110-μF ceramic capacitor bank that buffers current surges and permits soft startup of the device upon power-up, and (iii) a sensor module. The wireless device alone (i.e., except the sensing modules) consumes, on average, 322-μW power (115 μA at 2.8 V) (fig. S19). The POx uses two LEDs driven at a high current for short periods of time [5-mA and 250-μs pulse widths each, 50 samples per second (sps)], with an average power consumption of 336 μW. The surveillance monitor requires high current demands for longer periods of time (5-mA and 500-ms pulse widths), which consists in an average power consumption of 9 mW per sensing event (5 mA at 1.8 V) (fig. S20) or a 450-μW average power when operating at 0.1 sps. Although these systems operate under similar average power, the unique instantaneous power demand scenarios emphasize the capabilities of MAB as a versatile power supply for various IoT devices (see Materials and Methods for additional details). Figure S21 shows the electronic diagram of the demonstrator devices.

Wireless, wearable POx

Photoplethysmography, the basis for the POx device, uses transdermal differential spectroscopy (red: 638 nm; near-infrared: 936 nm; fig. S22) to measure relative concentrations of oxygenated and deoxygenated hemoglobin for estimating absolute levels of oxygen saturation (SpO_2) or relative levels of regional tissue oxygenation (StO_2). Figure 5A shows an exploded view of a MAB-powered POx consisting of two parts: (i) a reusable, lightweight (280 mg), wireless module encapsulated within a soft, silicone housing and (ii) a disposable skin adhesive membrane affixed with two series-connected MAB cells and a silicone gel. The silicone gel promotes optical impedance matching between the optoelectronic interface and the skin tissue. Thin neodymium micromagnets form robust reversible electromechanical connection between the cells and the module. The magnetic connection enables facile, on-demand replacement of the skin adhesive and battery (Fig. 5B) and maintains high fidelity during repeated attach/detach cycles (fig. S23), as well as under bending and inertial forces (fig. S24). These forces replicate real-world scenarios, such as those experienced by wearable devices applied on curvilinear skin surfaces and in ambulatory users. Figure S25 shows photographs of the two parts and the complete system. A mobile phone application interfaces with the wireless POx for real-time bidirectional data transfer, storage, analysis, and visualization and offers the user with programmable (continuous/intermittent) data recording feature (Fig. 5C). The complete POx system consumes 658 μW (322 μW for the wireless module and 336 μW for the POx module operating at 50 sps and a 2.5% duty cycle for near-infrared + red LED pulses of 0.25 ms in pulse widths).

Figure S26 and Fig. 5 (D and E) substantiate the importance of incorporating Gly into the separator to extend battery performance. The life span of the POx module powered by Gly-free MAB cells operating in an intermittent mode with a duty cycle of 16.6% (10 s ON and 50 s OFF) reveals that lower humidity levels support longer device operation (fig. S26), which could be attributed to suppressing corrosive effects of overhydration of the separator in an environment with high humidity. As shown in Fig. 5D, a MAB without Gly powers the POx for ~16 and 12 hours (ambient conditions: 25°C and 50% RH) when operating at two intermittent modalities with different duty cycles: 16.6 and 50% (5 s ON and 5 s OFF), respectively. The POx uses a sampling rate of 50 sps during the ON state in both intermittent modes. The duration of operation drops to ~10 hours if the device is running continuously. In contrast, the POx with MAB

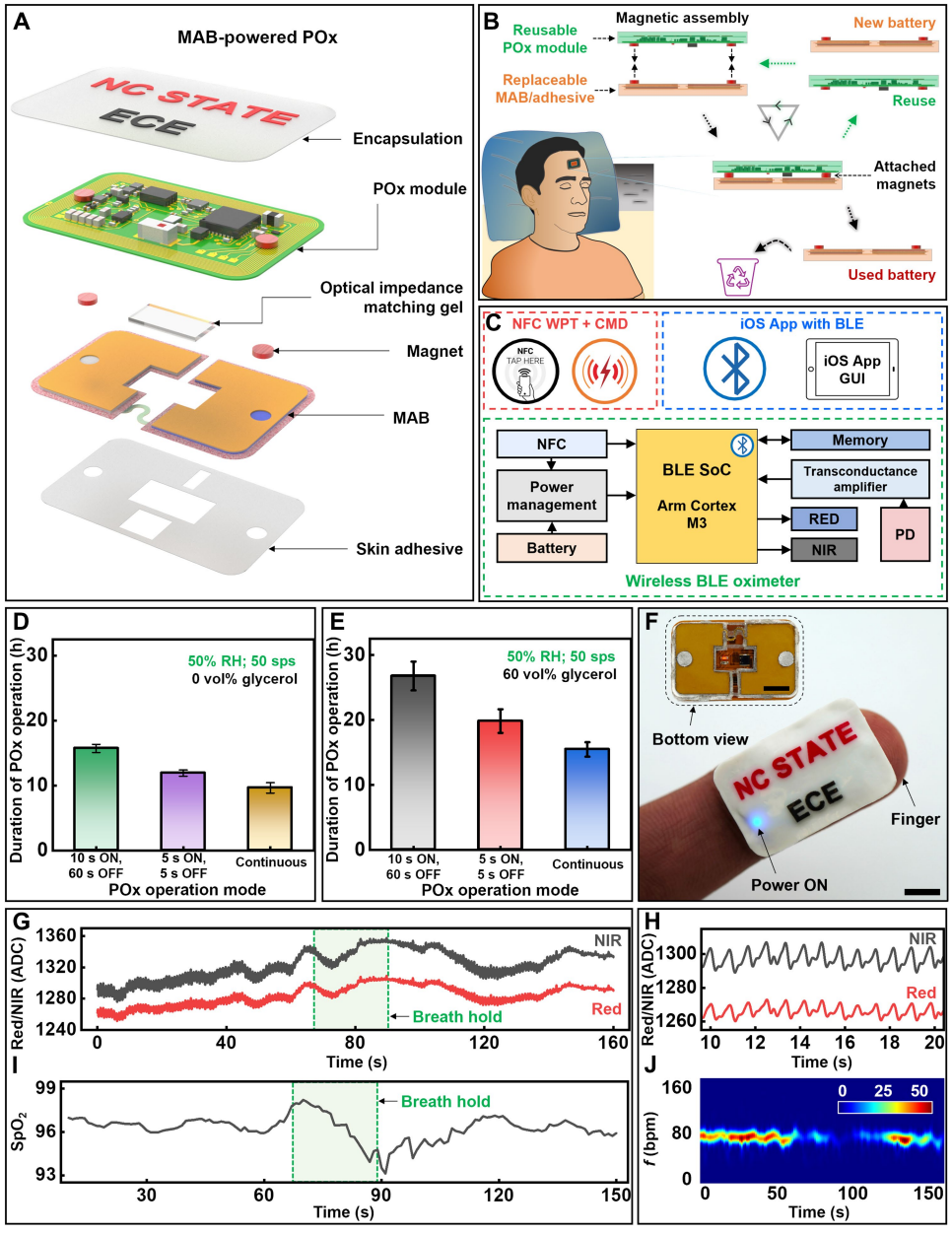

Fig. 5. MAB-powered, wearable, wireless POx. (**A**) Exploded view illustration of complete, wireless, wearable POx, detailing the structural design and constituent layers. (**B**) Illustration of magnet-assisted reversible attachment of the disposable battery/adhesive contingent to a reusable POx wireless electronic module. (**C**) System-level block diagram of the POx. The device supports data communication via BLE and data recovery from onboard memory using NFC (near-field communication) wireless power transfer to turn on the device. Operational life span of POx as a function of data sampling rate when powered by MAB containing a separator (**D**) without and (**E**) with 60 vol % Gly, tested at 25°C and 50% RH. (**F**) Photograph of fully assembled wearable POx applied to a human finger. The inset shows the bottom view of the POx. Scale bar, 5 mm. (**G**) Raw photodetector data collected at 50 sps from the fingertip of a human subject. (**H**) Raw photodetector data showing the pulsatile signature of the signal. (**I**) SpO_2 data estimated from the fingertip of a human subject. (**J**) Power spectrum of the near-infrared channel of the photodetector data showing the dominant frequency scaled to beats per minute. [(D) and (E)] Data are presented as the means ± SD; $n = 4$.

containing Gly within its separator runs for ~27 hours (16.6% duty cycle), ~20 hours (50% duty cycle), and ~16 hours (100% duty cycle) as shown in Fig. 5E, consistent with performance trends observed in Fig. 4F. While these studies are conducted under standard ambient conditions (25°C and 50% RH), Fig. 4F shows that the areal capacity of the MAB cells only slightly varies in the 30 and 70% RH range at 25°C, indicating that the POx should offer similar operational life span under such conditions as well.

A photograph of the POx attached to a human fingertip appears in Fig. 5F and is validated on a breath-hold exercise. Figure 5 (G to J) shows data collected during the test. Figure 5G shows the raw photodetector data, and Fig. 5H shows a snapshot of data depicting

the photoplethysmography signal. Figure 5 (G to I) shows the SpO_2 value estimated during this demonstration, and Fig. 5J shows the power spectrum. The data reveal that the subject's heart rate is ~70 beats per minute during the experiment.

Covert surveillance monitor with an inbuilt kill switch

The physical security of covert surveillance monitors is a major vulnerability in the intelligence community, as any compromise by an adversary could lead to jeopardizing of the operation. Equipping the monitors with an inbuilt kill switch that autonomously destroys the device and its data upon detecting physical tampering represents a unique route for covert intelligence gathering. Reported concepts of transient devices that undergo degradation when triggered by heat (*50*–*53*), light (*54*–*58*), ultrasound (*59*), water (*60*–*62*), or chemicals (*52*, *63*, *64*) could be used for realizing such monitors. However, these external triggers are not naturally present in normal environments, and the degradation rates of these devices are slow, on the scale of days to months. Also, they do not destroy the complementary metal-oxide semiconductor electronics. Collectively, these limitations impede the utility of these approaches in developing practical surveillance monitors with a fast-acting inbuilt kill switch.

The ambient moisture–harvesting concept that forms the basis of the MAB technology can be adapted to impart the desired zero-trust model into surveillance monitors. Figure 6A shows an image of such a monitor powered by two MAB cells each with a size of 1.56 cm by 1.2 cm (weight: 710 mg) connected in series. It includes a wireless environmental gas sensor (GSP41, Sensirion) that live-streams concentrations of ambient volatile organic compounds (selected as a model environmental analyte) via two types of BLE connection architectures: (i) a central-peripheral or (ii) broadcaster-observer (see Materials and Methods for more details). Figure 6B shows the sensor's reversibility to ethanol vapor. Figures S27 and S28 provide additional images of the monitor and its key components and schematics of BLE connection architectures, respectively. Figures S29 and S30 highlight the data demonstrating a linear response of the sensor to increasing ethanol vapor concentrations and power analysis for the monitor.

The surveillance monitor incorporates a chemical kill switch mechanism based on the highly exothermic reaction between elemental aluminum (Al) and iodine (I_2) in the presence of aqueous water. To prevent premature activation, a dry mixture of Al and I_2 (Al/I_2) powder is stored within a 3D-printed housing covered with a LiCl-impregnated cellulose membrane. The wireless monitor sits on top of the membrane.

Upon field deployment, the LiCl membrane rapidly captures ambient moisture and becomes fully hydrated. Under standard operating conditions, the monitor remains metastable because of the physical separation between the hydrated membrane and the underlying Al/I_2 powder. System destruction is triggered by external mechanical pressure (~4.3 kPa), e.g., unauthorized physical handling by an unsuspecting adversary, which facilitates direct contact between the hydrated membrane and the dry powder. This contact induces rapid transfer of water from the LiCl membrane to the underlying Al/I_2 powder, initiating a self-sustaining combustion reaction. The resulting fire is sufficient to achieve complete thermomechanical destruction of the integrated sensor and electronic components within 3 min. Control experiments conducted under high-humidity conditions (~70% RH) without the mechanical trigger show no observable thermal response or material degradation over extended periods, confirming that ambient humidity alone does not activate the kill switch.

Figure 6C conceptually illustrates the monitor in action and its autonomous self-destruction upon physical tampering, while Fig. 6D shows a zoomed-in schematic illustration highlighting the working principle of the kill switch mechanism. Figure 6E and figs. S31 and S32 present photographs of this process. Movies S3 and S4 capture the series of events leading to the monitor's complete destruction and the interruption of real-time data streaming between the monitor and the receiver (fig. S33), respectively. Table S6 highlights the superior performance of the monitor when compared to other reported examples of transient electronics for the purpose of realizing surveillance monitors with an inbuilt kill switch. The surveillance monitor with the inbuilt kill switch serves as a proof-of-concept application that leverages ambient moisture to function, similar to the MABs, thus illustrating the ability of the ambient moisture–activated mechanism to help realize various types of unconventional devices ranging from batteries to surveillance monitors.

DISCUSSION

We describe a previously unidentified class of nontoxic, MAB cells with performance comparable to or, in some cases, surpassing those of several widely used commercial, toxic cells. The battery owes its impressive performance to its unique working principle and choice of materials. The present work provides a comprehensive characterization of the battery, elucidating the underlying mechanisms governing its performance and stability. Demonstration of powering a wearable POx and an advanced surveillance monitor highlights the battery's ability to power energy-hungry IoT devices. The batteries open untapped opportunities in miniaturized, high-energy-density, and nontoxic power sources suitable for next-generation IoT devices. Future work should focus on avenues that help improve long-term storage stability of the cells, enable rapid cell activation, and expand the application of the MAB concept. Specifically, investigating unexplored electrode chemistries and separator compositions that enable repeated use of the MAB cells and facilitate the development of rechargeable analogs may extend the use of this technology to various use cases, including health care, human-machine interface, and distributed devices. In parallel, a geometry- and gradient-engineered capture zone that facilitates tunable moisture uptake kinetics and transport pathways without compromising mechanical compliance or electrochemical stability should be developed. Similarly, efforts should be made to make the kill switch in the surveillance monitor more robust, for example, by including multilayer encapsulation, humidity-responsive barrier films, and/or mechanically interlocked trigger structures, providing additional safeguards for long-term deployment in various environments.

MATERIALS AND METHODS

Fabrication of the MAB cell

CO_2 laser (Fusion Edge, Epilog, US) patterning (speed: 10%; power: 3.5%; frequency: 10%; cycles: 1) of a 30-μm-thick sheet of polyimide (PI; Argon Inc., CA) followed by screen printing of Ag conductive epoxy adhesive (MG Chemicals, Canada) formed the current collector/substrate for the anode and cathode. Subsequent attachment of manually excised 100-μm-thick Mg (Alibaba) foil using Ag epoxy on the current collector followed by baking at 120°C for 20 min

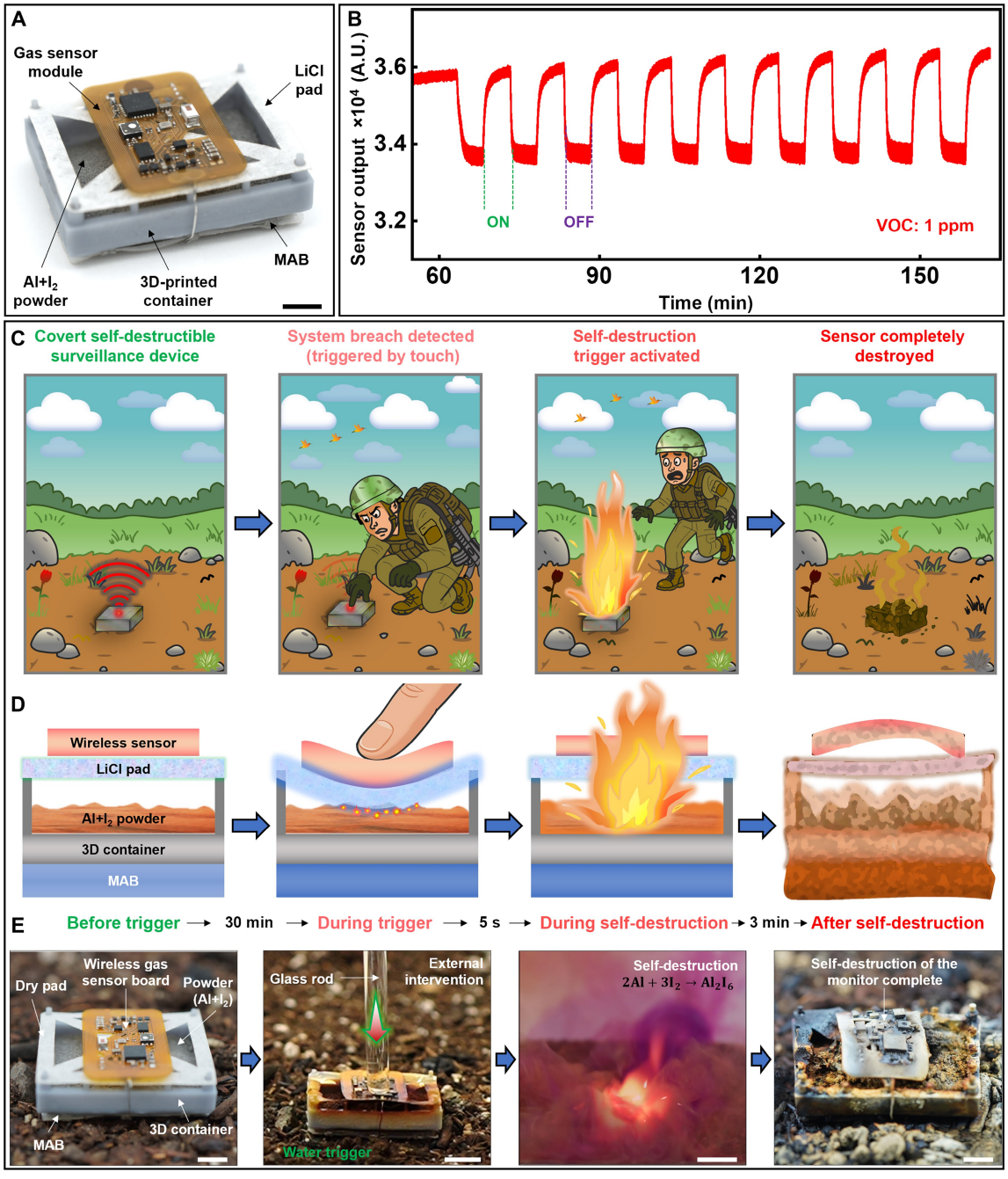

Fig. 6. MAB-powered, wireless surveillance monitor with inbuilt kill switch. (**A**) Photograph of the surveillance monitor with an inbuilt kill switch. (**B**) Wirelessly recorded response curves of the monitor to cyclical exposure to 1 ppm (parts per million) of ethanol vapor (10 cycles). A.U., arbitrary units. (**C**) Illustration showing key operational features of the monitor: active surveillance monitoring and self-destruction initiated by system breach. (**D**) Zoomed-in cross-sectional illustrations showing the working principle of the kill switch. (**E**) Photographs showing the monitor performing surveillance (here, measuring real-time, environmental volatile organic gas concentrations), being breached by external physical contact, and being destroyed after the kill switch is triggered. [(E), left and right] Scale bars, 5 mm. [(E), center-left] Scale bars, 1 cm. [(E), center-right] Scale bars, 2 cm.

formed the anode. Next, screen-printing Ag/AgCl ink (E2414, Ercon, US) onto a laser printer temporary tattoo paper (BubblePop, US) using a 500-μm-thick stencil, followed by baking at 120°C for 20 min and repeating the screen-printing step on the same stencil and baking at 120°C for an additional 30 min, formed a fully cured Ag/AgCl film. Subsequently, CO_2 laser patterning (speed: 10%; power: 10%; frequency: 10%; cycles: 5), detaching the cutouts from the tattoo paper by applying water to it, drying the cutouts at 120°C for 10 min, bonding them to the current collector using Ag epoxy, and subsequent baking at 120°C for 20 min formed the cathode. NaCl pad preparation involved depositing NaCl solution prepared in deionized water onto a CO_2 laser–patterned (speed: 10%; power: 2.5%;

frequency: 20%; cycles: 1) cellulose membrane (Kimtech Science Kimwipes, Kimberly-Clark Professional, US) followed by baking to evaporate water and repeating this process until a total of 2.4 mg/cm^2 NaCl salt is deposited. LiCl-based capture zone (areal loading of LiCl: 30 mg/cm^2) preparation followed a similar process. Motor grounding of 20 mg of HPC (average molecular weight: ~1000,000) powder (Sigma-Aldrich, US), 88 mg of XG powder (Anthony's Goods, US), and 1.5 ml of deionized water followed by vertexing for an hour yielded the gel. Applying the gel on both sides of the NaCl pad and baking it at 100°C for 5 min yielded the electrolyte zone. Placing the electrolyte zone over the capture zone completed the separator fabrication process. Next, placing the separator in between the anode and the cathode and subsequent encapsulation of the whole sandwich structure using a laser-patterned (speed: 10%; power: 3.5%; frequency: 10%; cycles: 1) 150-μm-thick PET membrane (Gorilla Glue Inc., OH) completed the MAB cell assembly process.

Fabrication of soft, stretchable MAB

Soft, stretchable battery fabrication began with mechanically excising Mg films (3.2 mm by 3.2 mm) and CO_2 laser processing of Ag/AgCl films (3.2 mm by 3.2 mm), NaCl pads (3.6 mm by 3.6 mm), LiCl pads (4.6 mm by 4.6 mm), and encapsulation membrane (5.7 mm by 5.7 mm). Laser processing of the encapsulation membrane defined 1.5-mm-diameter openings that served as contact points. Sandwiching all layers as described in the "Fabrication of the MAB cell" section resulted in the assembly of battery cells. Separately, laser patterning of Ag/PI films defined the top and bottom serpentine interconnects. Attachment of battery cells at designated contact points using Ag epoxy in a manner that allowed connecting a pair of parallelly connected eight cells in series completed the fabrication of the 4 × 4 cell array. Next, drop-casting a soft silicone elastomer (Ecoflex 00-30; Smooth-On Inc., PA; part A and part B, mixed with 5 wt % Silc-Pig silicone white pigment) into a 3D-printed mold and curing the prepolymer mixture at 70°C for 30 min, followed by CO_2 laser processing (speed: 10%; power: 5%; frequency: 10%; cycles: 1) for openings, yielded 300-μm-thick, soft, encapsulation layers. Placing the fully assembled 4 × 4 cell array in between the top and bottom silicone encapsulation layers, followed by application of a solution of uncured silicone (Ecoflex 00-35; FAST) around the periphery and ambient curing for 5 min, completed the encapsulation process. Screen-printing uncured silicone (Ecoflex 00-35; FAST) mixed with 5 wt % Silc-Pig red and 5 wt % Silc-Pig black onto the top encapsulation layer using a 100-μm-thick stencil, followed by ambient curing for 5 min, formed the NC STATE and ECE logos, respectively.

NCSU LED strip

The fabrication began with soldering eight LEDs (APT 201 C) in parallel onto a copper-patterned PI sheet. Next, attaching an NCSU (North Carolina State University) text laser-patterned (speed: 10%; power: 4%; frequency: 10%; cycles: 1) Teflon sheet and placing an additional Teflon sheet on top completed the light diffuser featuring the NCSU logo.

Fabrication of the AA-size MAB cell

Fabrication of a rectangular battery cell with dimensions of 4.86 cm by 20 cm followed the procedure similar to that described in the "Fabrication of the MAB cell" section. Separately, stereolithography three-dimensional (3D) printing (Saturn 3, Elegoo, US) of top and bottom caps, followed by Ag epoxy coating of inner and outer layers through holes, resulted in the current collector for the anode and cathode. Next, rolling the battery cell into a cylindrical form, inserting it between the caps, encapsulating the assembly in a soft silicone elastomer (Ecoflex 00-30; Smooth-On Inc. PA, part A and part B, mixed with 5 wt % white pigment) with NC STATE and ASSIST logos, and lastly attaching a humidity indicator (Humidity Detection Test Paper, Bartovation, US) pad on top of the LiCl pad completed the fabrication of an AA-size MAB cell.

Fabrication of the water transport study system

Laser patterning of cellulose membranes defined the pad structures of the capture zone and electrolyte zone, and their fabrication process followed the steps described in the "Fabrication of the MAB cell" section, except that the LiCl solution used for preparing the capture zone was colored with a red food dye.

Fabrication of the MAB-powered POx system

Fabrication of MAB

Fabrication of two MAB cells (15.6 mm by 12 mm) connected in series followed procedures similar to those described in the "Fabrication of the MAB cell" section. Laser processing of the PET membrane encapsulation defined 2-mm-diameter openings for bonding magnets (D1002-10, SuperMagnetMan, AL; diameter: 2 mm; thickness: 1 mm) using Ag epoxy. Next, laser-processing waterproof, double-sided skin adhesive bandage (Nuanchu, China) to define an opening that serves as an optical window for light interaction and subsequently attaching it to the bottom of the battery imparted the skin-bonding ability to the thin-film battery.

Fabrication of optical impedance matching gel

Gel fabrication involved drop-casting skin-safe silicone rubber gel (Ecoflex Gel; Smooth-On Inc., PA; part A and part B mixed at a 1:1 ratio) into a 3D-printed mold, vacuum-desiccating for 10 min to remove air bubbles, curing at room temperature for 2 hours, and razor blade cutting to yield a transparent, adhesive gel (3.7 mm by 7.7 mm).

Fabrication of the wireless POx module

Fabrication of the electronic circuit board began with designing the layout in Autodesk Fusion (Electronics package, Autodesk Inc.) followed by patterning of the design on a doubled-sided flexible printed circuit board (fPCB) by a third-party vendor (PCBWay, China). Figure S21 shows the electronic diagram. The fPCB consisted of a multilayer stack: PI coverlay (12.5 μm)/adhesive (15 μm)/copper (12 μm)/PI inner substrate (25 μm)/copper (12 μm)/adhesive (15 μm)/PI coverlay (12.5 μm), totaling 120 μm in thickness. Low-temperature soldering (SMD291SNLT6, Chip Quick Inc.) using a heat air gun (220°C) soldered the electronic component on the fPCB. A thin layer of Ag epoxy enabled affixing a pair of neodymium magnets (D1002-10, SuperMagnetMan, AL; diameter: 2 mm; thickness: 1 mm) to the contact pads of the electronic module with poles complementary to the pair attached to the MAB. Bonding the freestanding optical impedance matching gel to the LED and photodetector via a thin uncured gel resulted in firm attachment of the gel to the optic components, reducing optical losses. Last, encapsulating the electronic module within a thin, silicone membrane with openings to expose the magnets and the gel completed the fabrication process.

Calculation of SpO_2

The 12-bit analog-to-digital converted data from the red (RED) and near-infrared (NIR) channels, sampled at 50 sps, are used to calculate the SpO_2 using the ratio-of-ratio empirical model (*65*)

$$R = \left(\frac{\mathrm{RED_{rms}}}{\mathrm{RED_{dc}}}\right) / \left(\frac{\mathrm{NIR_{rms}}}{\mathrm{NIR_{dc}}}\right) \quad (1)$$

Here, $\mathrm{RED_{rms}}$ and $\mathrm{NIR_{rms}}$ are the root-mean-squared values of the alternating current (ac) components of both channels, and $\mathrm{RED_{dc}}$ and $\mathrm{NIR_{dc}}$ are the direct current (dc) components of both channels. The dc components of the data are extracted using a fourth-order low-pass Butterworth filter with a 0.2-Hz cutoff frequency. The ac components of the data are extracted using a fourth-order bandpass Butterworth filter with 0.5- to 2-Hz cutoff frequencies. The SpO_2 is then estimated using the following equation calibrated against a finger POx

$$\mathrm{SpO_2}(\%) = 122 - 26R \quad (2)$$

The SPO_2 data were computed in MATLAB, every second, using a 10-s moving window.

Fabrication of surveillance monitor with an inbuilt kill switch

The development of the monitor first involved fabrication of the MAB-powered volatile organic gas-sensing electronic module, which followed the procedure similar to that of the POx module. The module involved a commercial gas sensor chip (GSP41, Sensirion). Next, mixing Al (particle size: 35 μm; Artmolds, NJ) and I_2 (Sigma-Aldrich, MO) powders in 1:4 (w/w) proportions, loading it manually into a stereolithography 3D-printed housing (32 mm by 25.5 mm by 6.7 mm), and then placing the LiCl-based capture zone (LiCl loading: 30 mg/cm^2) to serve as the lid of the 3D-printed housing completed the fabrication of the trigger mechanism. Last, mounting the electronic module on top of the housing and electrically connecting it to MAB completed the fabrication of the surveillance monitor.

Wireless data communication for POx and surveillance monitor

BLE enables wireless communication using different connection architectures. The demonstration in this work uses three modalities of operation to show the versatility of the wireless sensing platform. The first modality uses a peripheral (POx wireless device)-central (iOS device) connection architecture. This modality enabled bidirectional communication, allowing data transmission from the device as well as the ability to update the device operation parameters and sensing modality (continuous or intermittent) via the smartphone application (iOS application) (see fig. S33). The second modality uses the broadcaster (wireless gas sensor)-observer (a BLE-enabled data logger)–facilitated wireless beacon operation designed for the surveillance monitor. Here, the devices broadcasted up to 8 bytes in the advertisement package. Two bytes served as unique device IDs, whereas the remaining 6 bytes represented three variables at a 16-bit resolution, with two of them used for transfer of sensor and device data (battery level and volatile organic compounds). A Bluetooth observer device running in Arduino UNO R4 WiFi read and filtered Bluetooth advertising packages, extracted the variables, and sent them over serial communication to an application in MATLAB App for logging [fig. S28, B and C, showing the GUI (graphical user interface)]. The third modality consisted of a stand-alone sensor logger that functions while the battery lasts (designed for covert applications involving the surveillance monitor). In this modality, gas sensor data can be stored in a 1-Mbit on-board memory, which has a capacity to store 15 days of data (three variables) at a sampling rate of one sample per minute. Data can then be retrieved via BLE connection (first modality described above) from the gas sensor powered via wireless power transfer. Figure S34 shows the logic diagram that captures these operation modalities.

Electrochemical, electrical, mechanical, and morphological characterizations

Electrochemical characterization leveraged a potentiostat (PalmSens4, PalmSens, NL) for open circuit potential, chronopotentiometry, and impedance spectroscopy measurements. Evaluation of battery discharge performance involved connecting the battery cells to a multichannel potentiostat (MultiPalmSens4, PalmSens, NL) under a constant discharge current of 1 mA/cm^2 and recording the cell voltage until the terminal voltage reached 1 V. EIS studies involved performing tests over a frequency range of 0.1 Hz to 100 kHz under a 10-mV sinusoidal signal at a 0-V dc bias. CV studies comprised a potential range of −1.3 to +1.3 V at a scan rate of 100 mV/s for four consecutive cycles. A custom test chamber comprising a humidifier (HUL535W, Honeywell, US), a dehumidifier (TP30WKN, Honeywell, US), and a digital humidity controller (IHC-200, INKBIRD, China) enabled controlling ambient humidity levels. Shaking experiments comprised placing the electronic modules on an orbital shaker (LE8S, Shengwin) operating at a specific rotation speed. All experiments are conducted in quadruplicate ($n = 4$), and results are reported as mean values with standard deviation (mean ± SD). A SU3900 variable pressure field-emission scanning electron microscope (Hitachi, Japan) facilitated reported surface morphologies, microstructure, and elemental quantity analysis. ICP-MS (Ultimate 3000 LC System, US) determined the elemental composition of the separator samples to study the diffusion of lithium ions from the capture zone to the electrolyte zone.

Mechanical modeling of stretchable MAB

Commercial finite element simulation software (ABAQUS 2023) modeled the mechanical response of the system and quantified local strain distributions within the battery architecture for complex mechanical loading conditions (e.g., stretching, bending, and twisting). The 3D quasistatic model comprising ~380,000 elements incorporated modular designs of the Ag horseshoe serpentine interconnects and the 4 × 4 multilayer block of the battery cell components. Adopting meshed architectures for the serpentines using four-node reduced-integration shell elements (S4R) with a uniform thickness of $t_s = 0.16$ mm and assigning six elements across the width ensured converged geometric and strain resolution. Discretization of the 3D multilayer block arrays using second-order modified tetrahedral elements (C3D10M) accurately captured complex mechanical deformations and ensured that the serpentine traces do not fail or fracture ($\varepsilon < 1\%$). Linear elastic material with Young's modulus of $E_{Ag} = 63$ GPa and Poisson's ratio of $\nu_{Ag} = 0.37$ modeled the Ag serpentines, while a homogenized, linear elastic formulation with $E_B = 1.7$ GPa and $\nu_B = 0.45$ modeled the multilayered battery array blocks.

Coupled electromechanical modeling of stretchable serpentine interconnects

A coupled mechanical-electrical finite element framework predicted changes in the electrical resistance of battery interconnects under mechanical loading. The approach involved first performing mechanical simulations in ABAQUS to capture the deformed configurations of the stretchable interconnects per methodology outlined in the "Mechanical modeling of stretchable MAB" section. Next,

importing the deformed serpentine geometries into COMSOL Multiphysics (version 6.2) using the Electric Currents in Shells (ecis) module enabled the analysis of the electrical properties of the geometries under mechanical deformations. Applying the same mesh structure and shell thickness from the mechanical model in the electrical domain ensured continuity and consistency across simulations. Equations 3 and 4 govern the electrostatic field in the thin serpentine interconnects (*66*).

$$\nabla_T \cdot \left(d_s \sigma E_T\right) = 0 \tag{3}$$

$$E_T = -\nabla_T V \tag{4}$$

where ∇_T is the transverse (surface) gradient operator, d_s is the effective surface thickness of the serpentine, $\sigma = 6.16 \times 10^7$ S/m is the electrical conductivity of Ag, V is the voltage, and E_T is the surface electric field.

Simulating electric potentials of 1 and 0 V at the two ends of the interconnects and using Ohm's law enabled the computation of the resistance along the conductive serpentine path. Analysis of three distinct mechanical deformation modes, (i) uniaxial stretching up to $\varepsilon_x = 190\%$, (ii) bending/folding by $U_x = 11.12$ mm to produce an out-of-plane folding effect, and (iii) twisting through $\phi = 360°$ and recording of changes in electrical resistance (ΔR) at intermediate loading steps, allowed the investigation of evolution of resistance as a function of complex deformation. Expressing applied loading as a normalized parameter relative to the maximum deformation value (i.e., $\frac{\varepsilon_x}{\varepsilon_{max}}$, $\frac{U_x}{U_{max}}$, $\frac{\phi}{\phi_{max}}$) allowed the comparison across various deformation modes.

Moisture absorption and water transport modeling

Diffusion modeling was performed to investigate the water absorption within the cellulose membrane environment. This modeling analysis provides quantitative insight into the time-dependent distribution of absorbed water under different initial concentration loading conditions and informs the design of devices that rely on controlled ionic release/migration through the membrane environment. A 3D model was constructed in COMSOL Multiphysics (version 6.2) using the Transport of Diluted Species (tds) module to simulate water molecule diffusion over time. The governing time-dependent partial differential diffusion equation that describes the physics of the system is (*67*)

$$\frac{\partial c_i}{\partial t} + \nabla \cdot \left(-D_i \nabla c_i\right) = 0 \tag{5}$$

where c_i is the concentration of water, D_i is the diffusion coefficient of the cellulose materials, and ∇ is the gradient operator. The LiCl layer was initialized with varying areal densities ρ_{LiCl} (mass per unit area) of 15, 20, 25, and 30 mg/cm^2 to evaluate how concentration gradients influence moisture absorption. The absorbed water concentration c_{H_2O} is a function of the areal density of LiCl in the capture zone, calculated by the relationship

$$c_{H_2O} = \left(K \rho_{LiCl}^2 + \frac{1}{4}\right) c_0 \tag{6}$$

where $c_0 = 55 \times 10^3$ mol/m^3 is the molar concentration of water molecules per volume, and $A = \frac{1}{1200}$ cm^4/mg^2 is a fitting constant, influenced by the RH and the LiCl molecule distribution in the capture zone, determined from the steady-state weight change curves to capture the effective moisture-absorption efficiency of LiCl. The initial concentration of water c_{H_2O} is applied as a Dirichlet boundary condition to model the interface between the capture zone and the atmosphere. The diffusion coefficient of the NaCl-cellulose and LiCl capture zone layer was defined as

$$D = D_0\left(1 - \alpha \frac{c_i}{c_r}\right) \tag{7}$$

where D_0 is the baseline diffusion coefficient in the dilute limit, c_i is the local LiCl concentration range from 15 to 30 mg/cm^2, and c_r is the reference concentration (typically at 30 mg/cm^2). $\alpha = 0.3$ is an experimentally calibrated term that captures macroscopic nonideal transport behavior because of swelling effects, reflecting the reduction in effective diffusivity as the membrane becomes saturated at higher concentrations. A diffusion coefficient of $D_0 = 2.4 \times 10^{-9}$ m^2 s^{-1} was used for 30% RH, and $D_0 = 6.5 \times 10^{-9}$ m^2 s^{-1} was used for 70% RH. The thickness of the NaCl cellulose layer is $t_{NaCl} = 0.1$ mm. To control the out-of-plane diffusion between the cellulose membrane and the LiCl + red dye layer, an ultrathin interfacial layer with a thickness of $t_l = 0.0012$ mm and diffusion of $D_l = 2.4 \times 10^{-13}$ m^2 s^{-1} is introduced, matching the optical concentration profiles observed in the experiments. A transient diffusion analysis was performed over a 120-min time interval, outputting data every 35 s. The total number of elements in the simulation is ~12,000 elements to ensure accuracy and numerical convergence.

Weight change in the membrane

The temporal weight change, Δm, in the capture zone was calculated by integrating the element volume density of water ρ_{H_2O} over the 3D diffusion domain Ω as

$$\Delta m = \int_\Omega \rho_{H_2O} \, dV \tag{8}$$

The element volume density of water is given by $\rho_{H_2O} = M_{H_2O} c_{H_2O}$, where M_{H_2O} is the molar mass of water, and c_{H_2O} is the concentration of water through the capture zone. Thus, the final temporal weight change due to water absorption and diffusion is given by the following volume integral evaluated over the diffusion domain of the capture zone

$$\Delta m = \int_\Omega M_{H_2O} c_{H_2O} \, dV \tag{9}$$

Supplementary Materials

The PDF file includes:

Figs. S1 to S34
Tables S1 to S6
Legends for movies S1 to S4
References

Other Supplementary Material for this manuscript includes the following:

Movies S1 to S4

REFERENCES

1. H. C. Ates, P. Q. Nguyen, L. Gonzalez-Macia, E. Morales-Narváez, F. Güder, J. J. Collins, C. Dincer, End-to-end design of wearable sensors. *Nat. Rev. Mater.* **7**, 887–907 (2022).
2. C. Zhao, J. Park, S. E. Root, Z. Bao, Skin-inspired soft bioelectronic materials, devices and systems. *Nat. Rev. Bioeng.* **2**, 671–690 (2024).

3. Y. Wang, H. Haick, S. Guo, C. Wang, S. Lee, T. Yokota, T. Someya, Skin bioelectronics towards long-term, continuous health monitoring. *Chem. Soc. Rev.* **51**, 3759–3793 (2022).
4. J. Bang, S. H. Choi, K. R. Pyun, Y. Jung, S. Hong, D. Kim, Y. Lee, D. Won, S. Jeong, W. Shin, S. H. Ko, Bioinspired electronics for intelligent soft robots. *Nat. Rev. Electr. Eng.* **1**, 597–613 (2024).
5. J. T. Licardo, M. Domjan, T. Orehovački, Intelligent robotics—A systematic review of emerging technologies and trends. *Electronics* **13**, 542 (2024).
6. S. Yin, D. R. Yao, Y. Song, W. Heng, X. Ma, H. Han, W. Gao, Wearable and implantable soft robots. *Chem. Rev.* **124**, 11585–11636 (2024).
7. M. O. Ojo, S. Giordano, G. Procissi, I. N. Seitanidis, A review of low-end, middle-end, and high-end Iot devices. *IEEE Access* **6**, 70528–70554 (2018).
8. M. Merenda, C. Porcaro, D. Iero, Edge machine learning for AI-enabled IoT devices: A review. *Sensors* **20**, 2533 (2020).
9. R. Chataut, A. Phoummalayvane, R. Akl, Unleashing the power of IoT: A comprehensive review of IoT applications and future prospects in healthcare, agriculture, smart homes, smart cities, and industry 4.0. *Sensors* **23**, 7194 (2023).
10. H. Ahn, D. Kim, M. Lee, K. W. Nam, Challenges and possibilities for aqueous battery systems. *Commun. Mater.* **4**, 37 (2023).
11. Y. Cho, J. E. Kim, M. Song, J. Hwang, E. Hwang, J. Kim, W.-J. Song, Progress and challenges in aqueous batteries: Exploring polymer electrolytes for extreme temperature resilience. *Small Methods* **9**, e01161 (2025).
12. H. Wang, L. Kang, K. Wang, M. Wei, P. Pei, Y. Zuo, B. Liang, Failure mechanisms and strategies toward flexible zinc-air batteries. *Adv. Funct. Mater.* **34**, 2407347 (2024).
13. X. Huang, H. Hou, B. Yu, J. Bai, Y. Guan, L. Wang, K. Chen, X. Wang, P. Sun, Y. Deng, S. Liu, X. Cai, Y. Wang, J. Peng, X. Sheng, W. Xiong, L. Yin, Fully biodegradable and long-term operational primary zinc batteries as power sources for electronic medicine. *ACS Nano* **17**, 5727–5739 (2023).
14. H. N. S. Aldin, M. R. Ghods, F. Nayebipour, M. N. Torshiz, A comprehensive review of energy harvesting and routing strategies for IoT sensors sustainability and communication technology. *Sens. Int.* **5**, 100258 (2024).
15. B. Zhang, W. Xu, L. Peng, Y. Li, W. Zhang, Z. Wang, Nature-inspired interfacial engineering for energy harvesting. *Nat. Rev. Electr. Eng.* **1**, 218–233 (2024).
16. N. T. Garland, R. Kaveti, A. J. Bandodkar, Biofluid-activated biofuel cells, batteries, and supercapacitors: A comprehensive review. *Adv. Mater.* **35**, e2303197 (2023).
17. A. J. Bandodkar, S. P. Lee, I. Huang, W. Li, S. Wang, C.-J. Su, W. J. Jeang, T. Hang, S. Mehta, N. Nyberg, P. Gutruf, J. Choi, J. Koo, J. T. Reeder, R. Tseng, R. Ghaffari, J. A. Rogers, Sweat-activated biocompatible batteries for epidermal electronic and microfluidic systems. *Nat. Electron.* **3**, 554–562 (2020).
18. J. Besnoff, H. Zhong, S. Su, R. Kaveti, N. Maiya, S. Krishna, N. T. Garland, A. J. Bandodkar, D. S. Ricketts, Sweat-powered, mm-scale, continuous-time sensor systems with Bluetooth Low Energy (BLE) backscatter. *IEEE Access* **12**, 190092–190101 (2024).
19. I. Huang, Y. Zhang, H. M. Arafa, S. Li, A. Vazquez-Guardado, W. Ouyang, F. Liu, S. Madhvapathy, J. W. Song, A. Tzavelis, J. Trueb, Y. Choi, W. J. Jeang, V. Forsberg, E. Higbee-Dempsey, N. Ghoreishi-Haack, I. Stepien, K. Bailey, S. Han, Z. J. Zhang, C. Good, Y. Huang, A. J. Bandodkar, J. A. Rogers, High performance dual-electrolyte magnesium–iodine batteries that can harmlessly resorb in the environment or in the body. *Energy Environ. Sci.* **15**, 4095–4108 (2022).
20. Y. Liu, X. Huang, J. Zhou, C. K. Yiu, Z. Song, W. Huang, S. K. Nejad, H. Li, T. H. Wong, K. Yao, L. Zhao, W. Yoo, W. Park, J. Li, Y. Huang, H. R. Lam, E. Song, X. Guo, Y. Wang, Z. Dai, L. Chang, W. J. Li, Z. Xie, X. Yu, Stretchable sweat-activated battery in skin-integrated electronics for continuous wireless sweat monitoring. *Adv. Sci.* **9**, e2104635 (2022).
21. X. Huang, Y. Liu, J. Zhou, S. K. Nejad, T. H. Wong, Y. Huang, H. Li, C. K. Yiu, W. Park, J. Li, J. Su, L. Zhao, K. Yao, M. Wu, Z. Gao, D. Li, J. Li, R. Shi, X. Yu, Garment embedded sweat-activated batteries in wearable electronics for continuous sweat monitoring. *NPJ Flex. Electron.* **6**, 10 (2022).
22. X. Tong, T. Hua, M. Xu, D. Yang, G. Xiao, S. Li, X. Cao, Y. Shao, An energy-autonomous wearable fabric powered by high-power density sweat-activated batteries for health monitoring. *Adv. Fiber Mater.* **7**, 254–265 (2025).
23. D. Li, J. Ju, G. Zhang, L. Pei, W. Gao, Y. Jian, W. Wang, T. Liang, Y. Qiao, Z. Lu, Stretchable sweat-activated yarn batteries with strain-insensitive power output for textile electronics. *Wearable Electron.* **2**, 237–249 (2025).
24. Y. Yuan, Y. Lu, T. Liang, H. Jia, L. Meng, Y. Zhu, J. Wang, T. Huang, P. Guan, L. Zhou, Y. Zhou, Z. Li, T. Wan, D. Chu, Advances in sweat-activated batteries for powering wearable electronics: Structures, materials, challenges, and perspectives. *J. Phys. Energy* **7**, 012001 (2024).
25. B. E. Conway, W. G. Pell, T.-C. Liu, Diagnostic analyses for mechanisms of self-discharge of electrochemical capacitors and batteries. *J. Power Sources* **65**, 53–59 (1997).
26. R. Holze, Self-discharge of batteries: Causes, mechanisms and remedies. *Adv. Mater. Sci. Technol.* **4**, 32–47 (2022).
27. H. Shan, P. Poredoš, Z. Chen, X. Yang, Z. Ye, Z. Hu, R. Wang, S. C. Tan, Hygroscopic salt-embedded composite materials for sorption-based atmospheric water harvesting. *Nat. Rev. Mater.* **9**, 699–721 (2024).
28. C. Atalay-Oral, M. Tatlier, Tailoring hydrophobicity vs. water capacity of adsorbents for adsorption applications: Role of composites. *Adsorption* **30**, 673–684 (2024).
29. N. K. Wally, E. Sheha, I. M. Morad, M. M. El-Desoky, Combined effects of LiCl addition and solvent-in-water approaches on aqueous magnesium-ion battery performance. *ACS Appl. Energy Mater.* **8**, 4441–4455 (2025).
30. H. Fan, Z. Zheng, L. Zhao, W. Li, J. Wang, M. Dai, Y. Zhao, J. Xiao, G. Wang, X. Ding, H. Xiao, J. Li, Y. Wu, Y. Zhang, Extending cycle life of Mg/S battery by activation of Mg anode/electrolyte interface through an LiCl-assisted $MgCl_2$ solubilization mechanism. *Adv. Funct. Mater.* **30**, 1909370 (2020).
31. X. Yang, Z. Chen, C. Xiang, H. Shan, R. Wang, Enhanced continuous atmospheric water harvesting with scalable hygroscopic gel driven by natural sunlight and wind. *Nat. Commun.* **15**, 7678 (2024).
32. H. Lu, W. Shi, J. H. Zhang, A. C. Chen, W. Guan, C. Lei, J. R. Greer, S. V. Boriskina, G. Yu, Tailoring the desorption behavior of hygroscopic gels for atmospheric water harvesting in arid climates. *Adv. Mater.* **34**, e2205344 (2022).
33. R. Kaveti, M. A. Jakus, H. Chen, B. Jain, D. G. Kennedy, E. A. Caso, N. Mishra, N. Sharma, B. E. Uzunoğlu, W. B. Han, T.-M. Jang, S.-W. Hwang, G. Theocharidis, B. J. Sumpio, A. Veves, S. K. Sia, A. J. Bandodkar, Water-powered, electronics-free dressings that electrically stimulate wounds for rapid wound closure. *Sci. Adv.* **10**, eado7538 (2024).
34. A. M. V. Mohan, N. Kim, Y. Gu, A. J. Bandodkar, J.-M. You, R. Kumar, J. F. Kurniawan, S. Xu, J. Wang, Merging of thin- and thick-film fabrication technologies: Toward soft stretchable "Island–Bridge" devices. *Adv. Mater. Technol.* **2**, 1600284 (2017).
35. R. Jiao, R. Wang, Y. Wang, Y. K. Cheung, X. Chen, X. Wang, Y. Deng, H. Yu, Vertical serpentine interconnect-enabled stretchable and curved electronics. *Microsyst. Nanoeng.* **9**, 149 (2023).
36. W. Wu, Stretchable electronics: Functional materials, fabrication strategies and applications. *Sci. Technol. Adv. Mater.* **20**, 187–224 (2019).
37. D. Lee, S.-B. Kim, T. Kim, D. Choi, J. H. Sim, W. Lee, H. Cho, J.-H. Yang, J. Kim, S. Hahn, H. Moon, S. Yoo, Stretchable OLEDs based on a hidden active area for high fill factor and resolution compensation. *Nat. Commun.* **15**, 4349 (2024).
38. Y. Lee, B. J. Kim, L. Hu, J. Hong, J.-H. Ahn, Morphable 3D structure for stretchable display. *Mater. Today* **53**, 51–57 (2022).
39. N. Kim, J. Kim, J. Seo, C. Hong, J. Lee, Stretchable inorganic LED displays with double-layer modular design for high fill factor. *ACS Appl. Mater. Interfaces* **14**, 4344–4351 (2022).
40. J. Xu, Y. Li, J. Wang, H. Liu, Q. Hou, R. Wang, T. Lang, B. Cui, H. Pan, Y. Chen, J. Quan, H. Yang, L. Li, Y. Liu, Screen-printed highly stretchable and stable flexible electrodes with a negative Poisson's ratio structure for supercapacitors. *Nanoscale* **15**, 1260–1272 (2023).
41. R. Herbert, H.-R. Lim, W.-H. Yeo, Printed, soft, nanostructured strain sensors for monitoring of structural health and human physiology. *ACS Appl. Mater. Interfaces* **12**, 25020–25030 (2020).
42. C. D. Díaz-Marín, L. Zhang, Z. Lu, M. Alshrah, J. C. Grossman, E. N. Wang, Kinetics of sorption in hygroscopic hydrogels. *Nano Lett.* **22**, 1100–1107 (2022).
43. D. Bilanovic, J. Starosvetsky, R. H. Armon, Cross-linking xanthan and other compounds with glycerol. *Food Hydrocoll.* **44**, 129–135 (2015).
44. Z. Qiu, Y. Zhang, Y. Li, J. Sun, R. Wang, X. Wu, Glycerol as a leveler on ZK60 magnesium alloys during plasma electrolytic oxidation. *RSC Adv.* **5**, 63738–63744 (2015).
45. I. A. Zubaidi, R. Jones, M. Alzughaibi, M. Albayyadhi, F. Darzi, H. Ibrahim, Crude glycerol as an innovative corrosion inhibitor. *Appl. Syst. Innov.* **1**, 12 (2018).
46. Z. T. Gossage, T. Furuichi, T. Hosaka, K. Shibuya, S. Komaba, Glycerol electrolytes for safer and more sustainable sodium ion batteries. *Green Chem.* **28**, 3119–3125 (2026).
47. K. Park, S. Kim, J. Kim, G. Seo, M. Baek, Y. Cho, J. Lee, J. W. Choi, Glycerol as a binder additive for low-resistance graphite anodes in lithium-ion batteries. *J. Electrochem. Soc.* **169**, 040558 (2022).
48. R. Adriana, Fitriani, A. T. Hayati, M. B. Arif, A. Nurjanah, J. Karunawan, A. Marlina, E. Yulianti, Q. Sabrina, A. Subhan, Sudaryanto, A. A. Kareem, R. W. N. Nugroho, D. N. Basir, S. T. C. L. Ndruru, Tuning the conductivity and flexibility of functionalized cellulose/PVA binary blend doped with lithium perchlorate and glycerol: A new paradigm towards solid polymer electrolytes. *J. Mol. Liq.* **433**, 127661 (2025).
49. H. Lin, Y. Yang, Y.-C. Hsu, J. Zhang, C. Welton, I. Afolabi, M. Loo, H.-C. Zhou, Metal–organic frameworks for water harvesting and concurrent carbon capture: A review for hygroscopic materials. *Adv. Mater.* **36**, e2209073 (2024).
50. C. W. Park, S.-K. Kang, H. L. Hernandez, J. A. Kaitz, D. S. Wie, J. Shin, O. P. Lee, N. R. Sottos, J. S. Moore, J. A. Rogers, S. R. White, Thermally triggered degradation of transient electronic devices. *Adv. Mater.* **27**, 3783–3788 (2015).
51. L. Teng, L. Li, J. Huang, S. Li, R. Hu, X. Zhou, H. Wang, Fully recyclable liquid-metal-based multi-layer thermally triggered transient electronic devices. *Adv. Mater. Technol.* **8**, 2201031 (2023).
52. N. Banerjee, Y. Xie, H. Kim, C. H. Mastrangelo, "Microfluidic device for triggered chip transience," in *2013 IEEE Sensors* (IEEE, 2013), pp. 1–4.
53. V. Gund, A. Lal, "Graphene-on-polymer flexible vaporizable sensor," in *2021 IEEE 34th International Conference on Micro Electro Mechanical Systems (MEMS)* (IEEE, 2021), pp. 521–524.
54. H. L. Hernandez, S.-K. Kang, O. P. Lee, S.-W. Hwang, J. A. Kaitz, B. Inci, C. W. Park, S. Chung, N. R. Sottos, J. S. Moore, J. A. Rogers, S. R. White, Triggered transience of metastable poly(phthalaldehyde) for transient electronics. *Adv. Mater.* **26**, 7637–7642 (2014).
55. S. Zhong, X. Ji, L. Song, Y. Zhang, R. Zhao, Enabling transient electronics with degradation on demand via light-responsive encapsulation of a hydrogel–oxide bilayer. *ACS Appl. Mater. Interfaces* **10**, 36171–36176 (2018).

56. M.-H. Oh, Y.-H. Kim, S.-M. Lee, G.-S. Hwang, K.-S. Kim, Y.-N. Kim, J.-Y. Bae, J.-Y. Kim, J.-Y. Lee, Y.-C. Kim, S. Y. Kim, S.-K. Kang, Lifetime-configurable soft robots via photodegradable silicone elastomer composites. *Sci. Adv.* **9**, eadh9962 (2023).
57. S. Zhong, H. C. Wong, H. Y. Low, R. Zhao, Phototriggerable transient electronics via fullerene-mediated degradation of polymer:fullerene encapsulation layer. *ACS Appl. Mater. Interfaces* **13**, 904–911 (2021).
58. O. Phillips, J. M. Schwartz, A. Engler, G. Gourdin, P. A. Kohl, "Phototriggerable transient electronics: Materials and concepts," in *2017 IEEE 67th Electronic Components and Technology Conference (ECTC)* (IEEE, 2017), pp. 772–779.
59. D.-M. Lee, M. Kang, I. Hyun, B.-J. Park, H. J. Kim, S. H. Nam, H.-J. Yoon, H. Ryu, H. Park, B.-O. Choi, S.-W. Kim, An on-demand bioresorbable neurostimulator. *Nat. Commun.* **14**, 7315 (2023).
60. S.-W. Hwang, H. Tao, D.-H. Kim, H. Cheng, J.-K. Song, E. Rill, M. A. Brenckle, B. Panilaitis, S. M. Won, Y.-S. Kim, Y. M. Song, K. J. Yu, A. Ameen, R. Li, Y. Su, M. Yang, D. L. Kaplan, M. R. Zakin, M. J. Slepian, Y. Huang, F. G. Omenetto, J. A. Rogers, A physically transient form of silicon electronics. *Science* **337**, 1640–1644 (2012).
61. Y. Gao, Y. Zhang, X. Wang, K. Sim, J. Liu, J. Chen, X. Feng, H. Xu, C. Yu, Moisture-triggered physically transient electronics. *Sci. Adv.* **3**, e1701222 (2017).
62. J.-W. Shin, J. Chan Choe, J. H. Lee, W. B. Han, T.-M. Jang, G.-J. Ko, S. M. Yang, Y.-G. Kim, J. Joo, B. H. Lim, E. Park, S.-W. Hwang, Biologically safe, degradable self-destruction system for on-demand, programmable transient electronics. *ACS Nano* **15**, 19310–19320 (2021).
63. V. Gund, A. Ruyack, K. Camera, S. Ardanuc, C. Ober, A. Lal, "Transient micropackets for silicon dioxide and polymer-based vaporizable electronics," in *2016 IEEE 29th International Conference on Micro Electro Mechanical Systems (MEMS)* (IEEE, 2016), pp. 1153–1156.
64. S. S. Pandey, N. Banerjee, Y. Xie, C. H. Mastrangelo, Self-destructing secured microchips by on-chip triggered energetic and corrosive attacks for transient electronics. *Adv. Mater. Technol.* **3**, 1800044 (2018).
65. P. D. Mannheimer, The light–tissue interaction of pulse oximetry. *Anesth. Analg.* **105**, S10–S17 (2007).
66. COMSOL, The AC/DC Module User's Guide, COMSOL 5.4 (2018).
67. COMSOL, COMSOL Multiphysics Reference Manual, COMSOL 5.4 (2018).
68. SoftBattery, Printed thin and flexible SoftBattery | Enfucell Oy; www.enfucell.com/softbattery.
69. SR726SW (397) 10 Pcs, Maxell; www.maxell.eu/product/sr726sw-397-10-pcs/.
70. Thin-Film Battery Part 133310002 | Molex; www.molex.com/en-us/products/part-detail/133310002.
71. Silver Oxide button cells | VARTA AG; www.varta-ag.com/fileadmin/varta/industry/downloads/products/silver-oxide/VA_Folder_Primary_Silver_Oxide_Button_Cell_02.pdf.
72. D. Filip, D. Macocinschi, M.-F. Zaltariov, B.-I. Ciubotaru, A. Bargan, C.-D. Varganici, A.-L. Vasiliu, D. Peptanariu, M. Balan-Porcarasu, M.-M. Timofte-Zorila, Hydroxypropyl cellulose/pluronic-based composite hydrogels as biodegradable mucoadhesive scaffolds for tissue engineering. *Gels* **8**, 519 (2022).
73. M. Zheng, J. Chen, K. B. Tan, M. Chen, Y. Zhu, Development of hydroxypropyl methylcellulose film with xanthan gum and its application as an excellent food packaging bio-material in enhancing the shelf life of banana. *Food Chem.* **374**, 131794 (2022).
74. S. Karki, H. Kim, S.-J. Na, D. Shin, K. Jo, J. Lee, Thin films as an emerging platform for drug delivery. *Asian J. Pharm. Sci.* **11**, 559–574 (2016).
75. C. H. Barty-King, C. L. C. Chan, R. M. Parker, M. M. Bay, R. Vadrucci, M. De Volder, S. Vignolini, Mechanochromic, structurally colored, and edible hydrogels prepared from hydroxypropyl cellulose and gelatin. *Adv. Mater.* **33**, e2102112 (2021).
76. J. Patel, B. Maji, N. S. H. Narayana Moorthy, S. Maiti, Xanthan gum derivatives: Review of synthesis, properties and diverse applications. *RSC Adv.* **10**, 27103–27136 (2020).
77. S. S. Jaffar, S. Saallah, M. Misson, S. Siddiquee, J. Roslan, S. Saalah, W. Lenggoro, Recent development and environmental applications of nanocellulose-based membranes. *Membranes* **12**, 287 (2022).
78. R. Sariboga, O. F. Sarioglu, Applications of cellulose-based nanomaterials for sustainability and therapeutics: A review. *ChemBioEng Rev.* **11**, e202300069 (2024).
79. W. Wei, J. Xu, W. Chen, L. Mi, J. Zhang, A review of sodium chloride-based electrolytes and materials for electrochemical energy technology. *J. Mater. Chem. A* **10**, 2637–2671 (2022).
80. S. Chudy, A. Makowska, R. Kowalski, Sodium chloride in food. *Foods* **14**, 2741 (2025).
81. R. A. Rahimi, S. H. Yahaya, M. S. Salleh, A comprehensive review of the use of sodium chloride (NaCl) in the development of the COVID-19 vaccine and medical applications. *Multidiscip. Rev.* **6**, 2023028–2023028 (2023).
82. L. Yin, H. Cheng, S. Mao, R. Haasch, Y. Liu, X. Xie, S.-W. Hwang, H. Jain, S.-K. Kang, Y. Su, R. Li, Y. Huang, J. A. Rogers, Dissolvable metals for transient electronics. *Adv. Funct. Mater.* **24**, 645–658 (2014).
83. R. Kaveti, J. H. Lee, J. K. Youn, T.-M. Jang, W. B. Han, S. M. Yang, J.-W. Shin, G.-J. Ko, D.-J. Kim, S. Han, H. Kang, A. J. Bandodkar, H.-Y. Kim, S.-W. Hwang, Soft, long-lived, bioresorbable electronic surgical mesh with wireless pressure monitor and on-demand drug delivery. *Adv. Mater.* **36**, e2307391 (2024).
84. H. Kim, E. Kim, C. Choi, W.-H. Yeo, Advances in soft and dry electrodes for wearable health monitoring devices. *Micromachines* **13**, 629 (2022).
85. M. S. Lee, A. Paul, Y. Xu, W. D. Hairston, G. Cauwenberghs, Characterization of Ag/AgCl dry electrodes for wearable electrophysiological sensing. *Front. Electron.* **2**, 700363 (2022).
86. P. Nadeau, D. El-Damak, D. Glettig, Y. L. Kong, S. Mo, C. Cleveland, L. Booth, N. Roxhed, R. Langer, A. P. Chandrakasan, G. Traverso, Prolonged energy harvesting for ingestible devices. *Nat. Biomed. Eng.* **1**, 0022 (2017).
87. X. Huang, D. Wang, Z. Yuan, W. Xie, Y. Wu, R. Li, Y. Zhao, D. Luo, L. Cen, B. Chen, H. Wu, H. Xu, X. Sheng, M. Zhang, L. Zhao, L. Yin, A fully biodegradable battery for self-powered transient implants. *Small* **14**, e1800994 (2018).
88. M. Karami-Mosammam, D. Danninger, D. Schiller, M. Kaltenbrunner, Stretchable and biodegradable batteries with high energy and power density. *Adv. Mater.* **34**, e2204457 (2022).
89. L. Wang, C. Lu, S. Yang, P. Sun, Y. Wang, Y. Guan, S. Liu, D. Cheng, H. Meng, Q. Wang, J. He, H. Hou, H. Li, W. Lu, Y. Zhao, J. Wang, Y. Zhu, Y. Li, D. Luo, T. Li, H. Chen, S. Wang, X. Sheng, W. Xiong, X. Wang, J. Peng, L. Yin, A fully biodegradable and self-electrified device for neuroregenerative medicine. *Sci. Adv.* **6**, eabc6686 (2020).
90. L. Yin, X. Huang, H. Xu, Y. Zhang, J. Lam, J. Cheng, J. A. Rogers, Materials, designs, and operational characteristics for fully biodegradable primary batteries. *Adv. Mater.* **26**, 3879–3884 (2014).
91. Y. J. Kim, S.-E. Chun, J. Whitacre, C. J. Bettinger, Self-deployable current sources fabricated from edible materials. *J. Mater. Chem. B* **1**, 3781–3788 (2013).
92. M. Tsang, A. Armutlulu, A. W. Martinez, S. A. B. Allen, M. G. Allen, Biodegradable magnesium/iron batteries with polycaprolactone encapsulation: A microfabricated power source for transient implantable devices. *Microsyst. Nanoeng.* **1**, 15024 (2015).
93. X. Jia, C. Wang, V. Ranganathan, B. Napier, C. Yu, Y. Chao, M. Forsyth, F. G. Omenetto, D. R. MacFarlane, G. G. Wallace, A biodegradable thin-film magnesium primary battery using silk fibroin–ionic liquid polymer electrolyte. *ACS Energy Lett.* **2**, 831–836 (2017).
94. X. Jia, C. Wang, C. Zhao, Y. Ge, G. G. Wallace, Toward biodegradable Mg–air bioelectric batteries composed of silk fibroin–polypyrrole film. *Adv. Funct. Mater.* **26**, 1454–1462 (2016).
95. Y. Lv, X. Liu, J. Liu, S. Wu, S. Sun, P. Wu, Y. Wang, Y. Ding, Implantable and bio-compatible Na-O_2 battery. *Chem* **10**, 1885–1896 (2024).
96. G. Li, E. Song, G. Huang, Q. Guo, F. Ma, B. Zhou, Y. Mei, High-temperature-triggered thermally degradable electronics based on flexible silicon nanomembranes. *Adv. Funct. Mater.* **28**, 1801448 (2018).
97. D.-M. Lee, N. Rubab, I. Hyun, W. Kang, Y.-J. Kim, M. Kang, B. O. Choi, S.-W. Kim, Ultrasound-mediated triboelectric nanogenerator for powering on-demand transient electronics. *Sci. Adv.* **8**, eabl8423 (2022).

Acknowledgments: This work was performed in part at the Analytical Instrumentation Facility (AIF) at NCSU, which is supported by the State of North Carolina and the National Science Foundation (award number ECCS-2025064). The AIF is a member of the North Carolina Research Triangle Nanotechnology Network (RTNN), a site in the National Nanotechnology Coordinated Infrastructure (NNCI). This work was performed in part by the Molecular Education, Technology and Research Innovation Center (METRIC) at NCSU, which is supported by the State of North Carolina. **Funding:** A.J.B. acknowledges support from Advanced Self-Powered Systems of Integrated Sensors and Technologies (ASSIST) Center Industry Seed Fund and Chancellor's Innovation Fund. R.A. acknowledges support from the Rice ENRICH Office and the seed grant from the Rice Space Institute. B.S. thanks TUBITAK for financial support through the 2219 International Postdoctoral Research Fellowship Program (1059B192300656). A.V.-G. acknowledges startup fund support from NCSU. **Author contributions:** Conceptualization: R.K., P.L., A.J.B., R.A., A.V.-G., B.J., B.E.U., and A.B.H. Methodology: R.K., P.L., A.J.B., R.A., A.V.-G., B.J., B.E.U., V.M., A.B.H., and A.B. Software: R.K., P.L., R.A., A.V.-G., and A.B. Validation: R.K., A.R.-K., P.L., R.A., A.V.-G., B.J., V.M., A.B.H., and A.B. Formal analysis: R.K., P.L., R.A., A.V.-G., M.A., V.M., and A.B.H. Investigation: R.K., B.Ş., A.R.-K., P.L., R.A., A.V.-G., B.J., B.E.U., M.A., G.N.G., V.M., and A.B.H. Resources: A.J.B., R.A., and V.M. Data curation: R.K., R.A., A.V.-G., G.N.G., and A.B.H. Writing—original draft: R.K., P.L., A.J.B., R.A., A.V.-G., and A.B.H. Writing—review and editing: R.K., P.L., A.J.B., R.A., A.V.-G., B.J., B.E.U., V.M., and A.B.H. Visualization: R.K., P.L., R.A., G.N.G., and A.B.H. Supervision: A.J.B., R.A., A.V.-G., and V.M. Project administration: R.K., A.J.B., R.A., and A.V.-G. Funding acquisition: A.J.B. and R.A. **Competing interests:** A.J.B., R.K., and A.B.H. have filed a disclosure on the moisture-activated battery and the kill switch technology from Noth Carolina State University, NC. The other authors declare that they have no competing interests. **Data, code, and materials availability:** All data and code needed to evaluate and reproduce the conclusions in the paper are present in the paper and/or the Supplementary Materials. All materials generated in this study are described in detail in Materials and Methods and are available upon reasonable request. Devices reported in the manuscript can be provided by the corresponding author (A.J.B.; email: ajbandod@ncsu.edu) pending scientific review and a completed material transfer agreement.

Submitted 25 November 2025
Accepted 20 May 2026
Published 1 July 2026
10.1126/sciadv.aee2065

ScienceAdvances

Safe, high-performance, moisture-activated batteries for powering next-generation Internet-of-Things devices

Rajaram Kaveti, Akshay Bhardwaj, Pei Liu, Ayemeh Bagheri Hashkavayi, Bhavya Jain, Adrian Rodriguez-Kattan, Mahaboobbatcha Aleem, Baha Erim Uzuno#lu, Gurudatt N. G., Bünyamin #ahin, Veena Misra, Raudel Avila, Abraham Vázquez-Guardado, and Amay J. Bandodkar

Sci. Adv. **12** (27), eaee2065. DOI: 10.1126/sciadv.aee2065

Science Advances (ISSN 2375-2548) is published by the American Association for the Advancement of Science. 1200 New York Avenue NW, Washington, DC 20005. The title *Science Advances* is a registered trademark of AAAS.